doi：10.17596/0004018

D/V CHIKYU "Cruise Report"
CK23-03

Time series analysis of the Nankai Trough slow slip by seafloor borehole observatory measurements

Off Kii-channel

Nov.06,2023-Nov.28,2023

Japan Agency for Marine-Earth Science and Technology
(JAMSTEC)

Cruise Information

- Cruise ID: CK23-03
- Name of vessel: D/V CHIKYU
- Title of cruise:
  Time series analysis of the Nankai Trough slow slip by seafloor borehole observatory measurements
- Chief Scientist
  Eiichiro Araki (JAMSTEC)
- Cruise period
  Nov. 06, 2023-Nov. 28, 2023
- Ports of departure / call / arrival
  Shimizu/Shimizu
- Research area
  Off Kii-channel
  - Research map

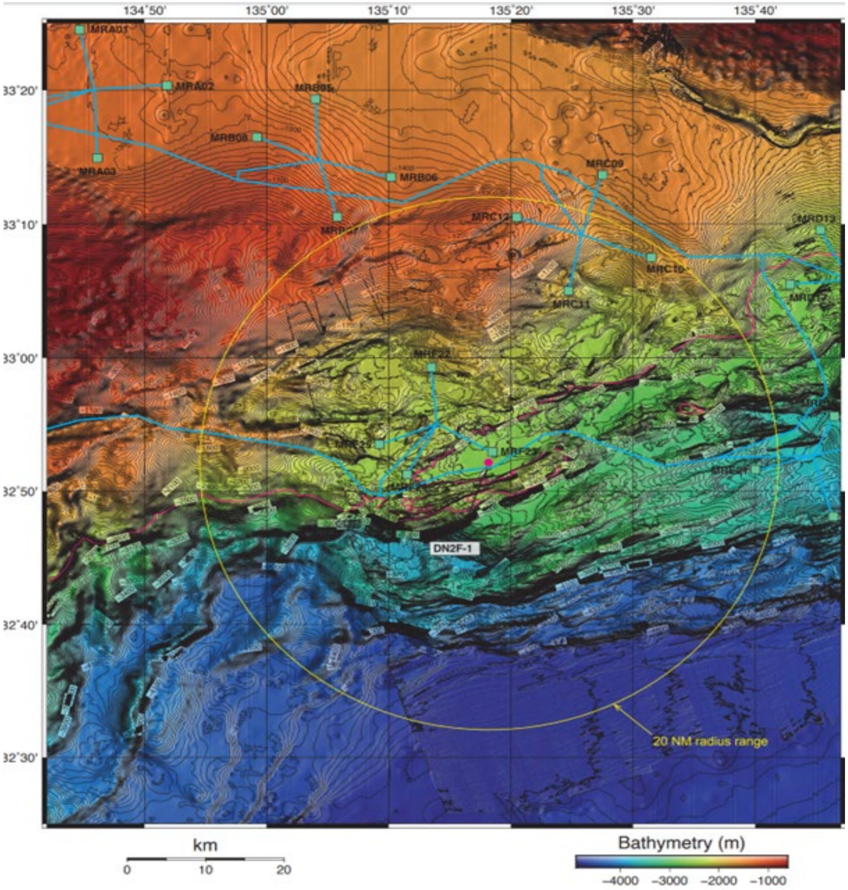

Hole no.	Latitude	Longitude	Depth [m]
C9038A	32°52.1365'N	135°18.1634'E	2,622.5
C9038B	32°52.1115'N	135°18.1652'E	2,620.5

Off Shikoku

- Research map

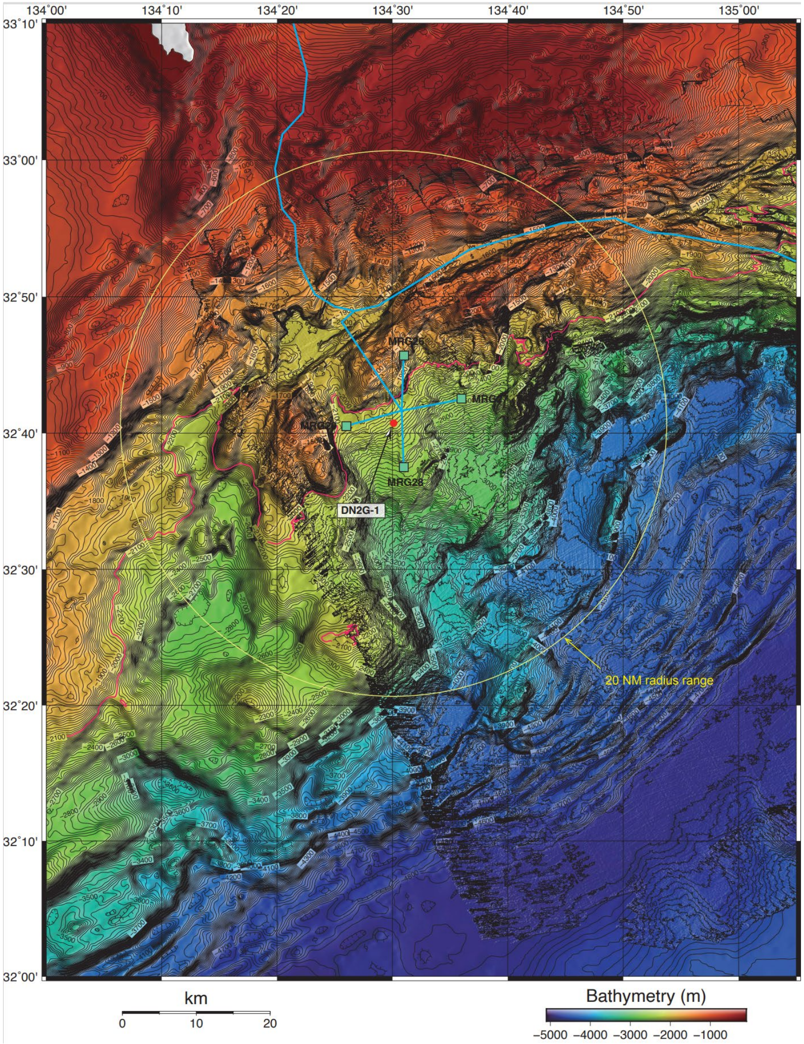

Hole no.	Latitude	Longitude	Depth [m]
C9039	32°40.6777'N	134°29.9926'E	2,265.0

1 Research Proposal and Science Party

- Title of proposal

Time series analysis of the Nankai Trough slow slip by seafloor borehole observatory measurements

● Representative of Science Party	Takane Hori	JAMSTEC
● Science Party	Eiichiro Araki	JAMSTEC
	Takashi Yokobiki	JAMSTEC
	Yuya Machida	JAMSTEC
	Shuhei Tsuji	JAMSTEC
	Satoru Baba	JAMSTEC
	Yohei Hamada	JAMSTEC
	Kaitlin Schaible	The University of Texas at Austin
	Masayuki Suzuki	JAMSTEC
	Masanori Kyo	JAMSTEC
	Tomokazu Saruhashi	JAMSTEC
	Noriaki Sakurai	JAMSTEC
	Takahiro Yokoyama	JAMSTEC
	Keita Akiyama	JAMSTEC
	Tatsuya Kaneko	JAMSTEC
	Lena Maeda	JAMSTEC
	Natsumi Okutsu	JAMSTEC
	Lena Murata	JAMSTEC

2 Research/Development Activities

2.1 Scientific objectives

Three borehole observatories have been installed in the Kumano-nado region of the the Nankai Trough megathrust seismogenic zone at three sites (Site C0002, C0010, and C0006) by the International Ocean Drilling Program (IODP). Long-term continuous observations of pore pressure and strain in the boreholes have revealed that slow slip repeatedly occurs at the shallow plate boundary offshore of the subduction zone (Araki et al., 2017 Fig. 1; Ariyoshi et al., 2021a, Fig. 2). Some of these offshore slow slip events repeat spontaneously, but some also appear to be induced by earthquakes in nearby and distant areas (Araki et al., 2017). According to the coupling analysis from the GNSS-A observations in the Nankai Trough area (Yokota et al., 2016, Yokota and Ishikawa, 2020, Fig. 3), there are correlations between the inter-plate coupling conditions and occurrence of slow slip events and slow earthquakes (Baba et al., 2020). In recent years, in-situ calibration of DONET seafloor pressure gauges has

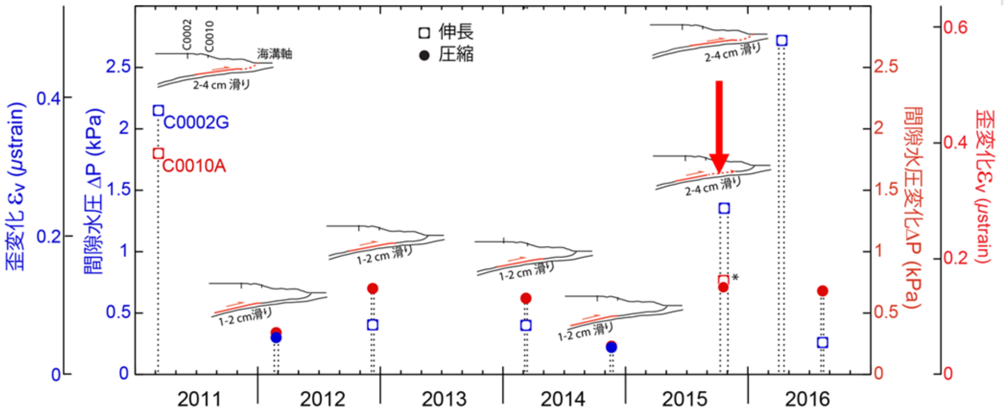

Fig. 1, Summary of pressure and strain transients at hole C0002G(blue) and C0010A(red) (after Araki et al., 2017).

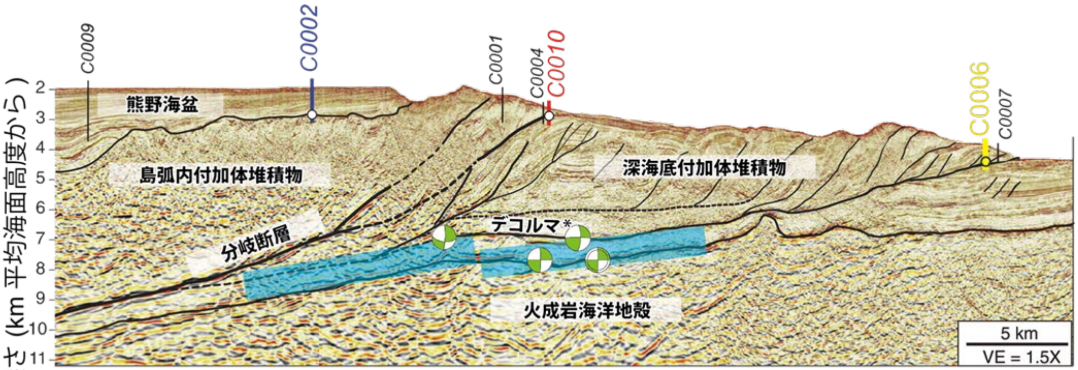

デコルマ* 潜り込む堆積物とはぎ取られる堆積物の境界のすべり面

Fig.2, Fault models that explains the slow slip event observed at the C0002, C0010 and C0006 borehole observatories. The focal depths of the fault models are assumed to be consistent with very low frequency earthquakes (VLFEs) (Ariyoshi et al., 2021b).

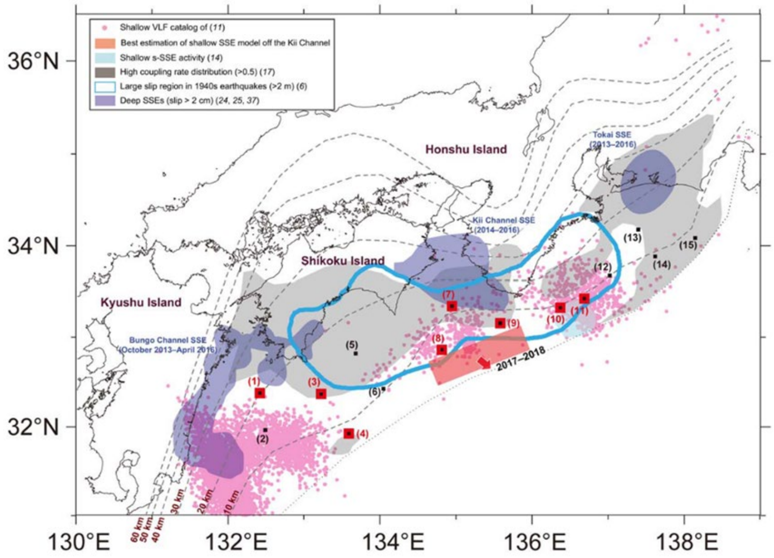

Fig. 3, Spatial relationship between seafloor site that detected SSE signals (red squares) and some phenomena along the Nankai Trough (after Yokota ane Ishikawa, 2020).

been conducted to understand the interplate coupling based on the vertical component of seafloor variations (Machida et al., 2020).

Furthermore, in areas of plate subduction associated with shallow slow earthquakes, their occurrence has been suggested to be related to structural factors at plate boundaries, such as seamount subduction (Shiraishi et al., 2020; Qin et al., 2020; Nakamura et al., 2022; Yamamoto et al., 2022). This may indicate that the structure of the stress field and fault strength between the plates resulting from structural factors make a slow-slip-like slip possible.

Analysis of drilling samples and data from D/V Chikyu collected in the area of shallow slow slip events have confirmed the existence of high pore-fluid pressure zones. These zones of highly pressurized water lenses may be involved in the occurrence of slow slip near the shallow plate boundary in the Nankai Trough off Muroto (Hirose et al., 2021). In addition, very-low-frequency seismic activity associated with slow-slip is observed to be related to the diffusion of subterranean fluids (Yamamoto et al., 2021). Changes in seismic wave propagation characteristics in the crust were also suggested. These may be related to the migration of underground fluids in slow-slip and slow-seismogenic areas (Tonegawa et al., 2022b).

In the Kumano-nada Nankai Trough, analysis of airgun seismic records obtained by the Chikyu borehole seismograph indicated that the physical properties of the fault beneath the seafloor may be tidally responsive (Tonegawa et al., 2021). However, the spatial extent of such analysis is limited to the area around the drilling area.

In other subducting zones, accelerated migration speed of local seismic activity was reported in association with an occurrence of slow slip just before the Tohoku earthquake (Kato et al., 2012), and a relationship between seamounts and slow earthquakes has also been suggested in Hikurangi (Barnes et al., 2020). Theoretical analyses of fault slip in the plate boundaries based on numerical simulations also reproduce the occurrence of slow slip event in the conditions of detached coupling and increased pore pressure (Ariyoshi, 2020).

Based on these findings, it is possible to: 1. Clarify the locations and mechanisms of shallow slow slip, slow earthquakes and their spatiotemporal distribution, 2. Analyze these slow-slip earthquake in conjunction with the plate boundary structure, to clarify the mechanism of strain accumulation and release at the boundaries of subducting plates that lead to large earthquakes.

On the other hand, the magnitude of repeated slow slip events observed in the borehole in the Kumano-nada area (Fig. 1) indicates that it is not easy to observe these slow slip events. Many of the slow slips observed in the boreholes so far, produce strain variations that are below the limit detectable by strain observations at the seafloor (~200 nstrain) (Araki et al., 2019)). It is clear that the actual situation of spatio-temporal behavior of the plate boundary cannot be covered only by seafloor observations.

Therefore, in order to understand the current state of plate coupling in areas of the Nankai Trough through covering repeated occurrence of slow slip events, we proposed to select three areas (between offshore Shikoku to the Hyuga Sea in the Nankai Trough) (Fig. 4) where slow slip is strongly expected to occur and deploy an ultra-high sensitivity borehole monitoring system capable of recording slow slip in these areas. The installation of the Long-Term Borehole Monitoring System (LTBMS) observatory at Site C9038 is the first site of three proposed sites to deploy these advanced borehole observation systems.

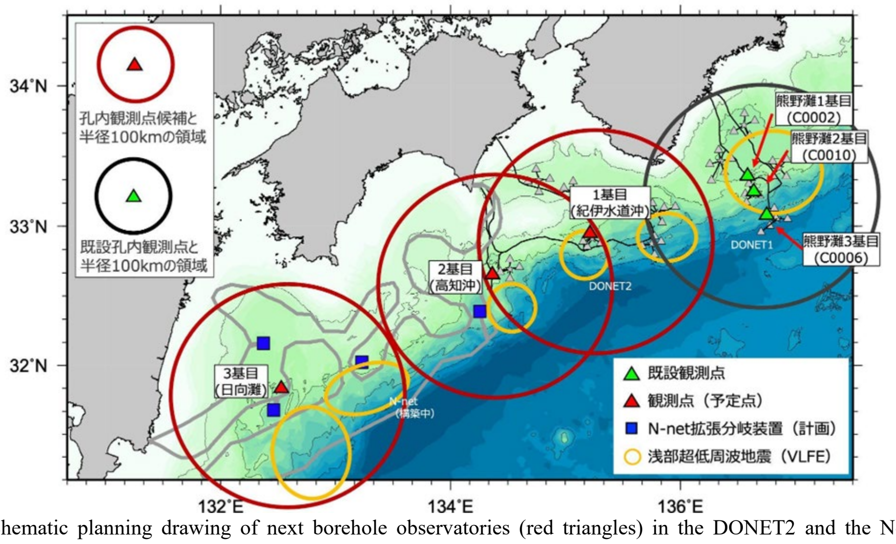

Fig. 4, Schematic planning drawing of next borehole observatories (red triangles) in the DONET2 and the N-Net area expanding westwardfrom theKumano-nada region (excerpt from the Ministry of Education, Culture, Sports, Science and Technology budget request material).

2.2 Site selection

The first target LTBMS site was chosen among the three target areas (DONET-2F, DONET-2G, N-Net Hyuganada; Figure 10), from the following reasons.

1) Network connectivity
   As we need to conduct real-time monitoring of slow slip event, existent submarine cable network within reach from the site was mandatory. DONET-2F, and DONET-2G are in operation and ready to be connected while N-Net is currently in construction phase and connection node point is not existent nor fixed. We selected two candidate sites each of which connection cable distance shorter than 9km from DONET science nodes 2F and 2G (network connection point).
2) Background observation maturityFfi
   In DONET-2F area, seafloor fiber optic strainmeter is in operation and observation of slow slip event in 2022 Jan-Mar. helped to prioritize DONET-2F area to add new LTBMS to form an array strain observation which has been proven very effective to model slow slip area (Araki et al., 2017).
   In both DONET-2F, and 2G area, we observed repeated activities of VLFE and LFT swarms and therefore expectable for coexisting SSEs.
3) Feasibility of drilling completion.
   In order to make the expected performance of the LTBMS sensing for SSE detection, we need to drill a deep borehole so that strainmeter is cemented in stiff-enough formation and pore-fluid pressure is measured in less compliant and permeable zone just below the strainmeter depth. It is also required to maintain integrity of the hole long-time enough to reenter LTBMS string in, after drilling it to the target depth. Therefore, we excluded any accretionary prism from our target site! We needed to identify deep enough sediment basin or slope sediment formation extending down at least to 500 mbsf to choose sites.

We searched site location which fulfill all these criteria and we determined that DN2F-1 as primary target and DN2G-1 as alternative target we can aim for installing new LTBMS during the expedition.

2.3 Long-term Borehole Monitoring System (LTBMS)

2.3.1 Borehole fiber optical strainmeter

The LTBMS was developed to observe fault and crustal dynamics off the Kii Peninsula using instrumentation in a sub-seafloor borehole designed to detect slow slip events. The LTBMS measures multiple parameters such as ground motion, crustal deformation, and hydrogeological processes in a partially cased borehole approximately 500 m deep (Fig. 5). Within the borehole, a fiber optical strainmeter is installed which can observe precise strain changes by measuring the change in length of a 200 m optical fiber in a sensing part relative to the same length of reference fiber with a resolution of 1 nm. The sensing section consists of a 200m optical fiber helically wound around a stainless-steel mandrel (Fig. 6, 7). The sensing fiber cable is counted starting from the point where it is coiled at regular intervals around the stainless tube, and the fiber cable is wound around 399 and 5/6 turns in total (Fig. 8). In addition, an attempt will be made to suppress the absolute orientation of the fiber winding by painting the frame at the beginning of the fiber winding and checking its orientation with the ROV during installation.

Fig. 9 shows the fiber route of the borehole fiber optical strainmeter. The borehole fiber optic strainmeter is connected to a borehole/DONET interface, located on the remotely

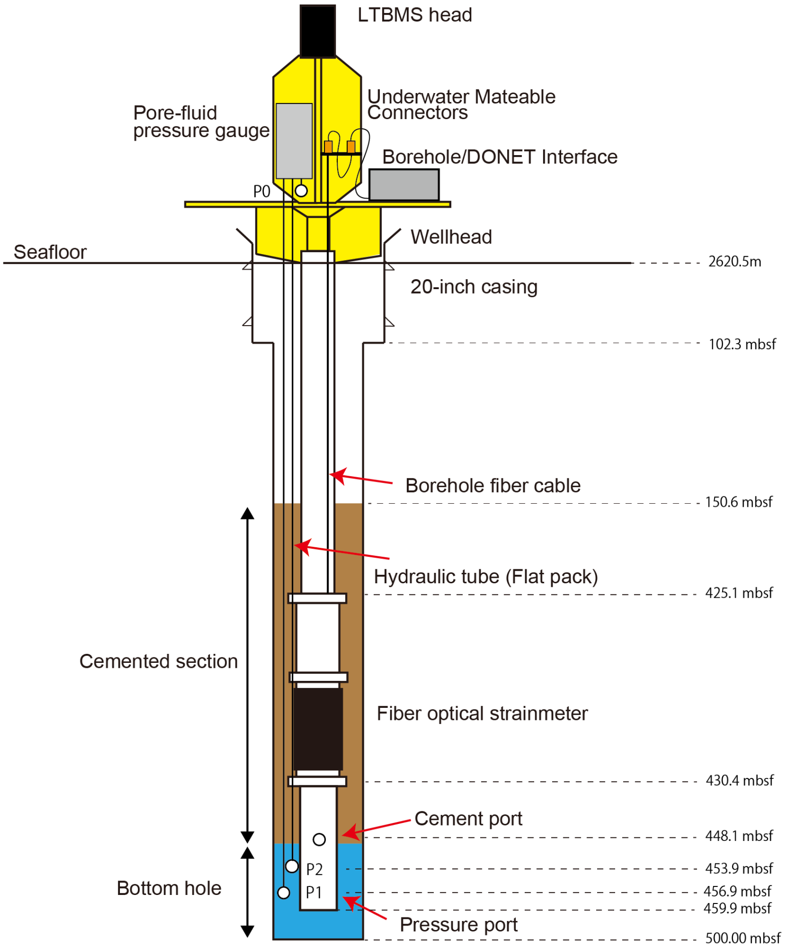

Fig. 5, Schematic of the DN2F-1 LTBMS system.

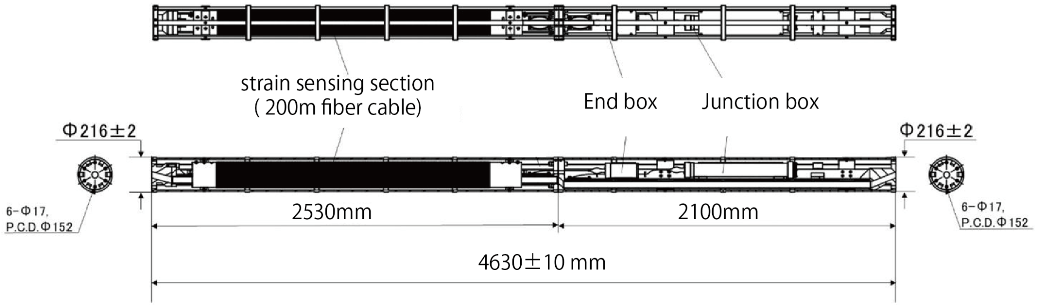

Fig. 6, Schematic of the borehole fiber optical strainmeter.

operated vehicle (ROV) platform, through the borehole fiber cable (Fig. 10), and the sensing fiber cable is connected between the junction box and the end box (Fig. 11). In the sensing fiber cable, fibers for strain measurement are fixed in the stainless tube by a glue. For this reason, it is possible to measure strain and temperature change by coupling with

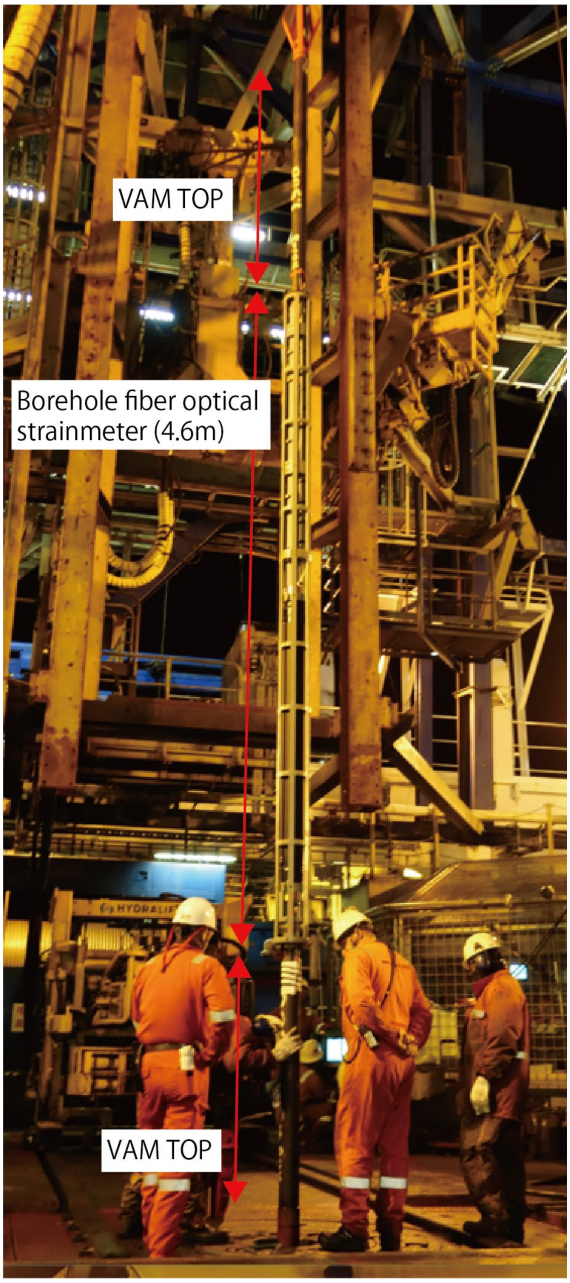

Fig. 7, Photograph of the borehole strainmeter on the rig floor before lowering to the moonpool.

surroundings. On the other hand, the fiber, which performs temperature measurement, has a slack inside the stainless tube, and can only measure the temperature.

The borehole fiber optical strain meter emits a laser beam from the logger in the borehole/DONET interface, and measures the difference in optical path length between the reference fiber and the sensing section beyond the 3x3 coupler in the junction box. The borehole fiber optical strain meter uses two types of fibers with different temperature coefficients: single mode fiber and PS1250. This is to differentiate between strain changes and temperature changes. For example, if a change due to strain is observed in the borehole, the same strain change is measured in both fibers. However, if there is a temperature change within the borehole, such as due to a change in the fluid path, the two fibers will measure a strain change proportional to the difference in temperature coefficient. The strain changes associated with SSEs are small and take place over long timescales, which is similar to temperature changes due to fluids in subduction zones. Therefore, it is important to measure strain changes accurately.

Vortex-induced vibration (VIV) is a common effect of the strong Kuroshio Current (Kitada et al., 2013), and operating in the current causes damage to equipment and sensors. VIV exhibits a dominant frequency of 3-15 Hz and a maximum acceleration of 2G. Vibration tests approximating these conditions were performed to confirm that the strainmeter design is capable of withstanding these vibrations during installation. Also, a protector was attached to the section where the fiber sensing cable of the borehole fiber optical strainmeter was exposed on the borehole wall side to prevent damages to the cable during lowering. In addition, the sensing cables were arranged so that the cement flow would not hit the cables directly and cause a load during cementing the process.

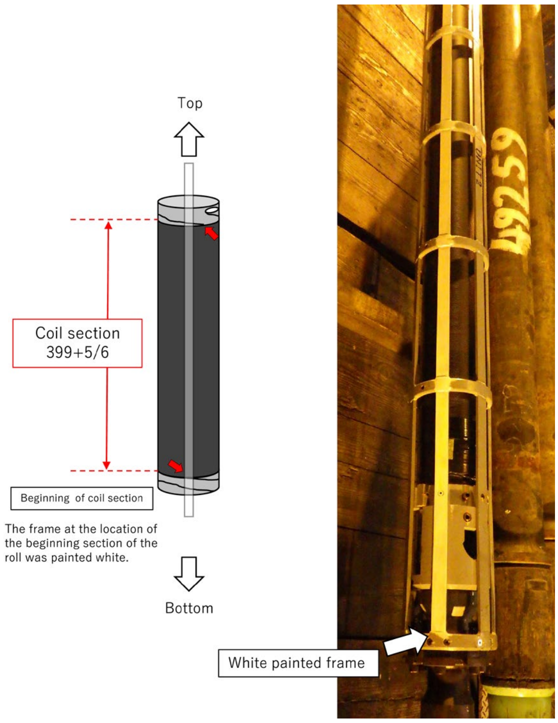

Fig. 8, Starting position of optical fiber cable winding

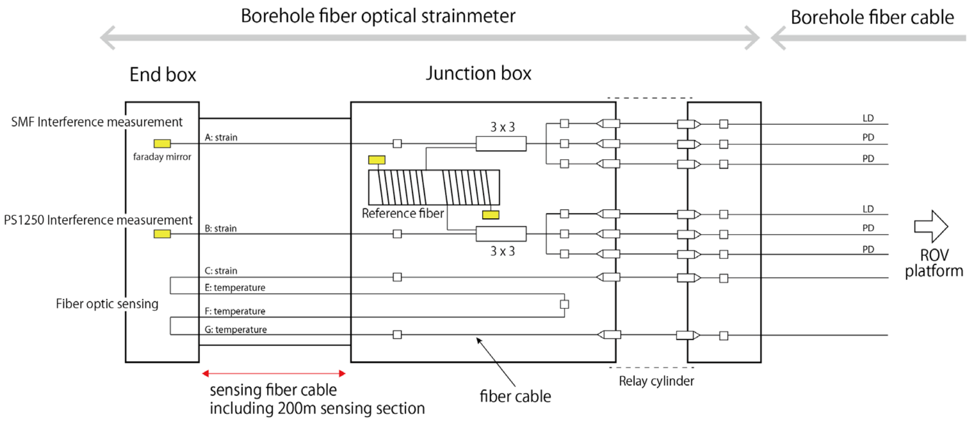

Fig. 9, Fiber route inside the borehole fiber optical strainmeter

2.3.2 Fiber optic sensing

The LTBMS system can also perform distributed fiber optic sensing such as distributed acoustic sensing (DAS) and Tunable Wavelength Coherent Optical Time Domain Reflectometry (TW-COTDR). The borehole fiber optical strainmeter has two types of optical fibers for interference measurement, as well as a fiber for optical sensing measurement (Fig.9). The fiber for optical sensing measurement measures over an 800m section by making two round trips through the sensing section. Of these, the section for strain measurement is 200m, and the section for temperature measurement is 600m. The initial condition of optical fiber in the LTBMS is

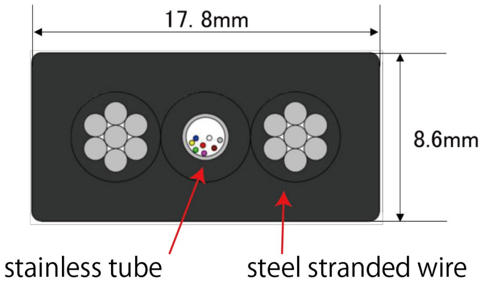

Fig. 10, Cross section of the borehole fiber cable.

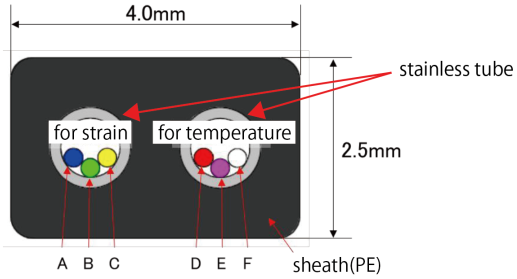

Fig. 11, Cross section of the fiber optic cable.

measured by DAS and TW-COTDR technique.

We conducted DAS and TW-COTDR measurements using the fiber-optic cables after the LTBMS was installed(Fig. 12). For DAS measurement, we used the model of AP Sensing (N5225B). The measurement setting is shown in Table 1. For TW-COTDR measurement, NBX-7033 and onsite by NEUBREX are used for measurement and postprocessing, respectively. The measurement settings are shown in Table 2.

Downhole sensing cable within the LTBMS was connected via ROV (Magnum 113 by OCEANEERING, Fig. 13). The laser pulse used for optical sensing is emitted by each instrument and transmitted to the borehole/DONET interface via a fiber optic cable and the ROV umbilical cable. The measurement instruments were set in the ROV container. From the ROV container, the laser runs through the umbilical cable and is composed of the 1st cable, between the ship and the ROV cage, and the 2nd cable, between the ROV cage and ROV. A wet-mate connecter and an ROV optical interface are installed on the ROV in order to collect data from the borehole fiber optic cable through the LTBMS interface. After going through the borehole fiber-optic cable, the laser passes through the sensing section in the borehole fiber optical strainmeter, and goes back to the borehole fiber cable again. The total length of fiber optic cable consists of multiple sections, including; 1st cable (4000 m), 2nd cable (380 m), the downhole borehole fiber optic cable (500 m), and the fiber-optic cable within the sensor package (~ 800 m).

The DAS measurement was conducted before (Test #7) and after cementing (Test #8). During DAS measurements, optical power loss was measured by optical time domain reflectometry (OTDR, Fig. 14). The large loss parts after pulsive peaks correspond to several connections.

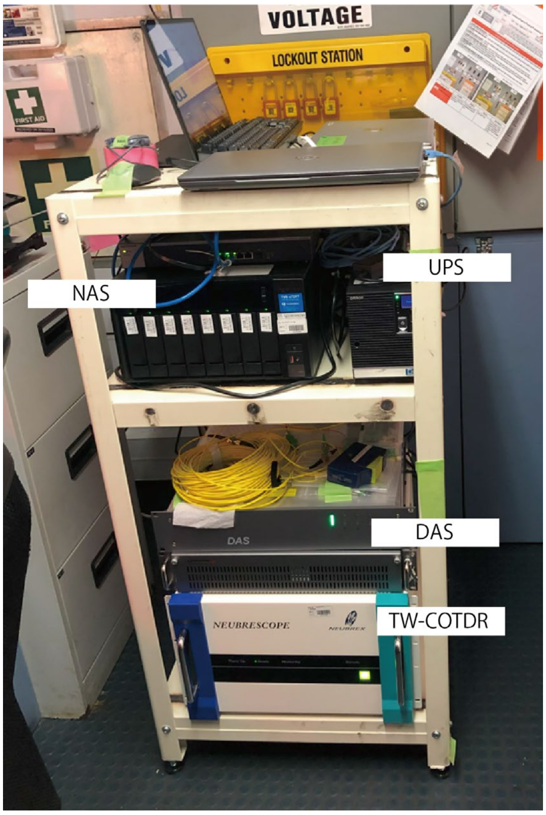

Fig. 12, The DAS unit and the TW-COTDR unit in the ROV container.

The TW-COTDR measurement was also conducted before (Test 7) and after cementing (Test #8). Parameters used for these observations are listed in Table 2.

Table 1. DAS measurement setting before installation of sensors

Sampling rate	4,000 Hz
Gauge Length	39.2 m
Spatial Sampling	4.9 m
Fiber length	13 km

Table 2. TW-COTDR measurement settings

Distance Range	13 km
Spatial sampling interval	10 cm
Spatial Resolution	1 m
Average count	8192
Output Pump Power	26 dBm
Span / step of sweep	30.000 GHz / 0.100 GHz

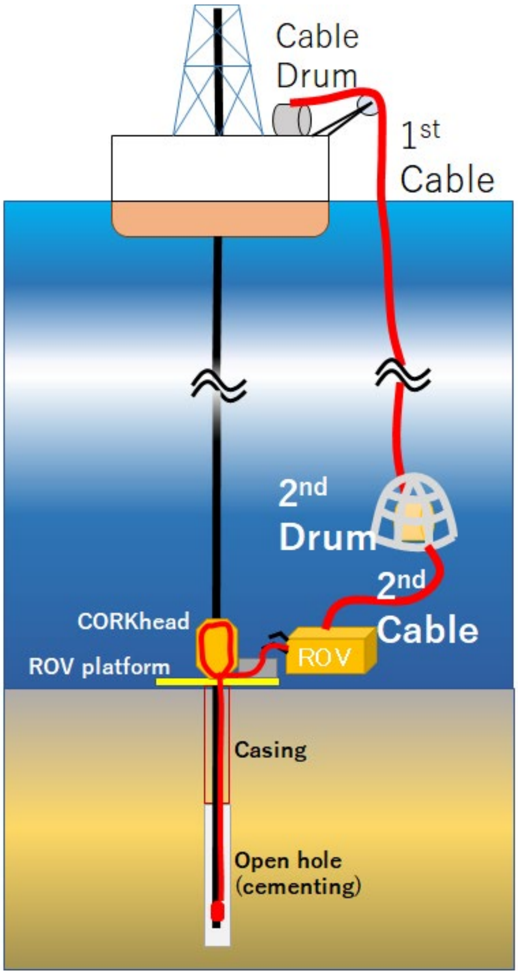

Fig. 13, Schematic of cable connections from Chikyu to borehole fiber optical strainmeter.

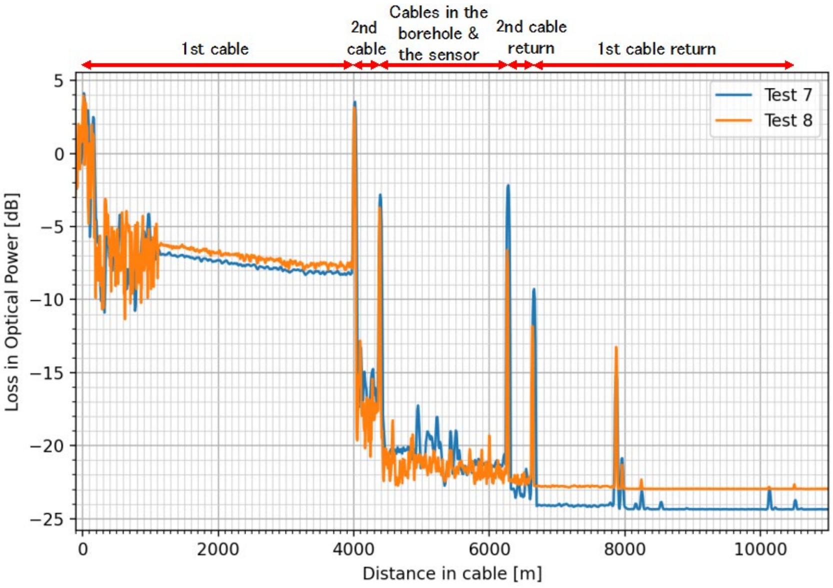

Fig. 14, Loss in the optical power by OTDR test. Blue and orange lines represent loss in the optical power of Test 7 and 8, respectively.

2.3.3 Pore-fluid pressure measurement

A pressure sensing unit (PSU) designed for multi-level monitoring of pore pressure was deployed during CK23-03 as part of the LTBMS (Fig. 15). The PSU is equipped with three Paroscientific Digiquartz pressure transducers (Model 410K-184; serial numbers 157228, 157229, 157230) and intelligence boards. The Paroscientific gauges have been widely used in other LTBMS systems and have proven to be accurate and reliable, with accuracy within ±0.01% of the full-scale range and pressure resolution to ± 1 ppb of full scale (Becker and Davis, 2005). Two transducers connect to ¼ inch stainless steel tubing that terminates at two measurement points in the subseafloor, downhole Pressure 1 (P1) and Pressure 2 (P2). The third transducer measures the seafloor pressure and temperature, Pressure 0 (P0). The two ¼ inch hydraulic lines for downhole pressure sensing are housed in flatpack umbilical that connects the subseafloor intervals to the LTBMS head. The borehole interval from 460 to 500 mbsf is

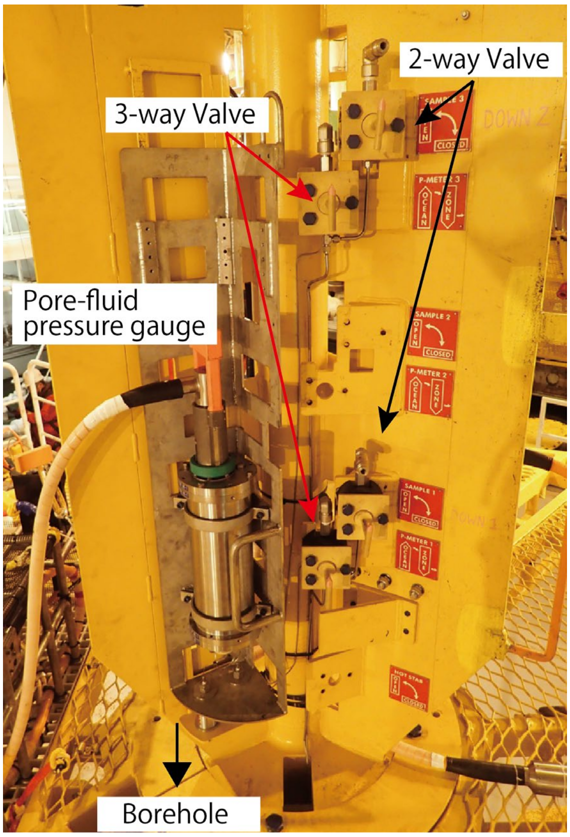

Fig. 15, Photograph of the pore-fluid pressure gauge

Fig. 16, Photograph of miniscreens.

spotted with PROTECTZONE VP to prevent cement from penetrating the pressure sampling interval. The borehole is cemented from 100 to 450 mbsf which isolates the screened interval and allows for monitoring of in situ formation pressures once disturbance from operations has dissipated.

The downhole monitoring intervals are located at the bottom of the open borehole at 457 mbsf (P1) and 454 mbsf (P2). Each pressure monitoring port is protected from clogging by three 1 inch diameter mini-screens that are 120° apart and are plumbed to a single manifold that connects to ¼ inch stainless steel hydraulic tube (Fig. 16). The two hydraulic tubes run through the instrument carrier above, and ultimately terminate at the LTBMS head where pressure is measured by two of the sensors in the PSU. The third sensor in the PSU is open to the ocean and measures a reference pressure at the seafloor (P0). The PSU is housed in the Valve bay of the wellhead (Fig. 15), and the data logger within the PSU can be accessed through an ODI Teledyne Underwater Mateable Connector (UMC). The ODI connector has a pin layout that is compatible with the other UMC's in the connector bay and allows the ROV pilot to use the same interface for communication and data download.

Prior to installation of the PSU on the LTBMS CORKhead, we conducted a draft test of the PSU in the laboratory. We measured the pressure from each transducer with a dead-weight type pressure balance for approximately one month to understand the long-term drift components of the transducers. The two transducers with the minimum and maximum drift components were selected as the downhole pressure transducers (P1 – S/N 157229, P2 – S/N 157230). The remaining transducer (S/N 175228) had a relatively small drift component and was selected to measure the seafloor pressure.

A few days before installation, we flushed the lines on the LTBMS CORK head and checked the plumbing and valve function (Fig. 17). For each formation pressure line, there is a two-way valve and a three-way valve that control the exchange of pressure to the PSU. The two-way valve is either "OPEN" or "CLOSED" and the three-way valve is either "OCEAN" or "ZONE". The "OPEN" position connects the downhole hydraulic lines to the seafloor pressure and the "CLOSED" position isolates the hydraulic lines to the PSU which enables measurement of the downhole formation pressure. The "OCEAN" position on the three-way valve enables measurement of the seafloor pressure by the PSU and allows for future calibration of the formation pressure transducers. The "ZONE" position isolates the downhole hydraulic lines to the PSU to measure formation pressure. After checking valve function, we performed a pressure check of the hydraulic lines on the LTBMS head. We used a hand pump to pressurize the lines to ~ 10 MPa and waited for 2 hours. We inspected each line for leaks and then released the pressure.

The day before LTBMS installation, we attached the PSU to the CORK head and bled air from the hydraulic lines. We performed the following procedure for P1 and P2:

1- Set the valve position to "CLOSED" and "OCEAN" and connect a hand pump to the hydraulic lines at the bottom of the CORK head.
2- Apply water pressure and ensured flow from the top of the three-way valve.
3- Switch the three-way valve to "ZONE" and allow steady water flow from the joint at the base of the PSU.
4- While water is flowing from the hydraulic line, connect to the base of the PSU. Stop applying water pressure when the pump registers pressure above atmospheric levels.

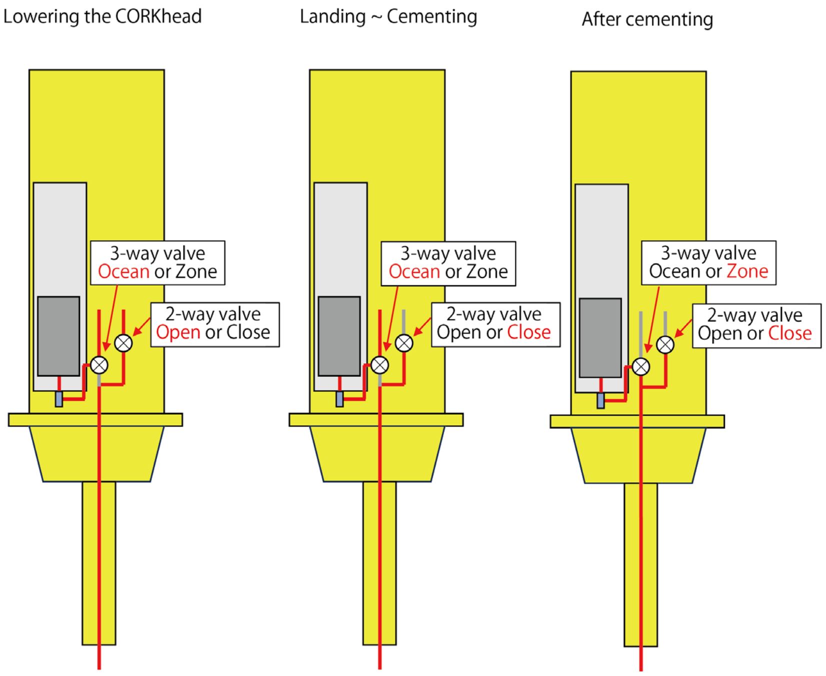

Fig. 17, Schematic diagram of valve status during installation.

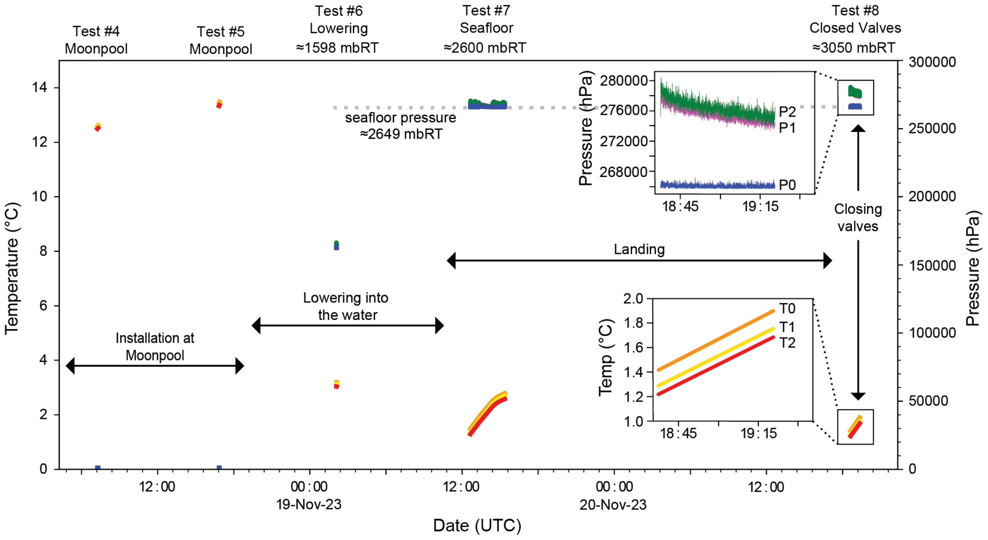

Fig. 18, Pressure and temperature record of the pore-fluid pressure gauge during a series of operation check. T0, T1 and T2 show a seafloor temperature recorded by the three pressure transducers. P0 is a seafloor pressure. P1 and P2 are the pressure at the bottom of the pressure ports (see Fig.1).

5- Tighten the joint at the base of the PSU firmly.
6- The valves should be in "CLOSED" and "ZONE" positions.

Before lowering the CORK head into the water, we changed the valve position to "OPEN" and "OCEAN" while the CORK head was on the moonpool. This allowed for air inside the hydraulic lines to escape as the LTBMS was lowered to the seafloor. Once the CORK head landed on the wellhead, we used the ROV to switch the valves to "CLOSED" and “OCEAN” to prevent mud and cement from entering the hydraulic lines. Approximately two hours after cementing, we switched the three-way valve to “ZONE” and began measuring formation pressure.

During the duration of the LTBMS construction and installation, we conducted five sensor health checks on the PSU to ensure function. See Fig. 18 for more details.

2.4 LTBMS Installation

2.4.1 Drilling

The 20" CSG and 10-5/8" drill pipe were lowered to the seafloor from the D/V Chikyu, and jetting began at the DN2F-1 observatory at midnight on November 9, 2023 (WD 2651.0 mBRT/2622.5 mbsl, Location: 32°52.1365'N, 135°18.1634'E). The 20" casing reached 48m below the seabed, and after conducting a slump test, the wellhead and 10-5/8" drill pipe were separated using a HART tool. At this time, the ROV's camera confirmed that wellhead was located about 5 meters above the ocean floor. Then, the 10-5/8" drill pipe strings were drilled down to 3151mBRT. However, when the wellhead was confirmed using an ROV camera after drilling, it was found to have sunk below the sea floor. This is probably because the surface ground is very soft, and the 20" CSG inserted 48mbsf was not able to maintain the holding force. Therefore, it was decided to move the excavation position 48m to the south and conduct excavation again. At this time, a 20" casing was installed approximately 100m below the seabed.

The next jetting began at midnight on November 14, 2023 (WD 2649.0 mBRT/2620.5 mbsl, Location: Lat: 32°52.1115'N, Long: 135°18.1652'E). At that observatory, 102m of 20" CSG was inserted and a slump test was performed. After confirming that the wellhead was retained, the wellhead and 10-3/5" drill pipe were separated using a HART tool. After that, we drilled down to 3149 mBRT and retrieved the 10-3/5" drill pipe strings to the wellhead. Then lowered the 10-3/5" drill pipe string to the bottom of the borehole again to check the condition inside the hole. Stagnation in the borehole was removed by mud circulation, and Protect Zone was inserted at the bottom to prevent cement from dripping, and 10-3/5" drilling pipe strings were

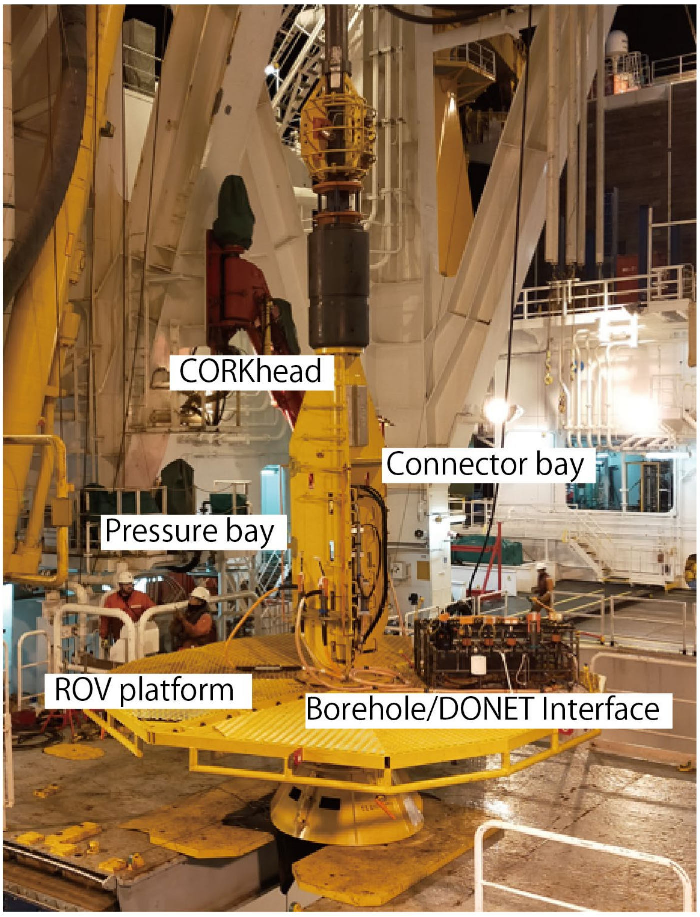

Fig. 19, Photograph of the assembled CORKhead and ROVplatform.

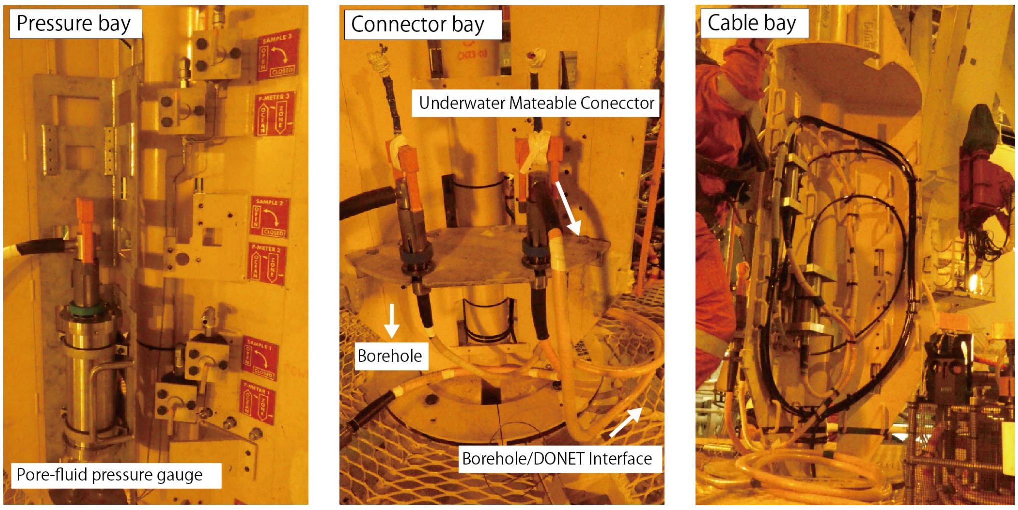

Fig. 20, Three bays set up at CORKhead (the pressure bay, the connector bay, and the cable bay)

recovered.

2.4.2 Installation

We started the LTBMS installation from midnight on November 17, 2023. The bull nose, the 4-1/2" TBGs, and the borehole fiber optical strainmeter were assembled on the rig floor and lowered to the moonpool. On the moon pool cart, a miniscreen installation and fiber connections of the borehole fiber optical strainmeter were carried out on a workbench called RGR until midnight on November 18th. Afterwards, the 4-1/2" TBGs were connected one after another, and the connector and sensor cable end were assembled to the CORKhead with the sensor at approximately 490 mBRT. After the pore-fluid pressure gauge, the borehole fiber cable, the ODI connectors, and the borehole/DONET interface were assembled on the CORKhead and the ROV platform (Fig. 19, 20), the LTBMS system started lowering into the borehole at midnight on November 19. The bull nose re-entered the hole C9038B (WD: 2649.0 mBRT/2620.5 mbsl, Location: Lat: 32°52.1115'N, Long: 135°18.1652'E), and the CORK head landed on the wellhead around noon on November 19th. Then cement was injected from the cement port above the water pressure measurement section. After that, the CORK head was disconnected from the pipe and the installation of the LTBMS system was completed around 07:00 on November 20th.

During deployment (assembly, lowering, re-entry, landing, cementing) a series of tests were conducted on the borehole fiber optical strainmeter and the pore-fluid pressure

Borehole fiber optical strainmeter

No.	Time (UTC)		Place	sensor depth (m)	remarks
	start	end			
1	11/17/23-05:15	11/17/23-06:22	moon pool	0	after sensor connection
2	11/17/23-13:53	11/17/23-14:04	moon pool	0	before sensor lowering
3	11/18/23-01:14	11/17/23-01:32	moon pool	460	before cable termination
4	11/18/23-06:16	11/18/23-07:05	moon pool	460	after cable termination
5	11/18/23-16:30	11/18/23-16:45	moon pool	460	before installation
6	11/19/23-01:49	11/19/23-02:00	ROV container	2060	while lowering
7	11/19/23-11:54	11/19/23-12:04	ROV container	3060	before cementing
8	11/20/23-17:15	11/20/23-18:27	ROV container	3060	after cemeting

Table 3. List of the Borehole fiber optical strainmeter operation test.

gauge to verify the health of the sensors (Table3, 4, and 5). Next, we will discuss the results of the tests carried out during installation for each sensor.

Pore-fluid pressure gauge

No.	Time (UTC)		Place	sensor depth (m)	remarks	Tools
	start	end				
4	11/18/23-07:10	11/18/23-07:21	moon pool	460	after cable termination	DC24V, ROV I/F
5	11/18/23-16:45	11/17/23-16:54	moon pool	460	before installation	DC24V, ROV I/F
6	11/19/23-02:02	11/19/23-02:09	ROV container	2060	while lowering	**ROV**, ROV I/F
7	11/19/23-12:36	11/20/23-15:22	ROV container	3050	before cementing	**ROV**, ROV I/F
8	11/20/23-18:36	11/18/23-19:21	ROV container	3050	after cemeting	**ROV**, ROV I/F

Table 4. List of the pore-fluid pressure gauge operation test.

DAS

No.	Time (UTC)		Place	sensor depth (m)	remarks
	start	end			
5	11/18/23-16:55	11/17/23-17:07	ROV container	450	SP=5m, GL=20m, PW=10m
5	11/18/23-17:09	11/17/23-17:11	ROV container	450	SP=5m, GL=20m, PW=10m
7	11/19/23-18:08	11/20/23-18:10	ROV container	3050	SP=5m, GL=20m, PW=10m
7	11/19/23-18:17	11/20/23-18:19	ROV container	3050	SP=5m, GL=20m, PW=10m
7	11/19/23-18:19	11/20/23-18:23	ROV container	3050	SP=5m, GL=40m, PW=20m
7	11/19/23-18:24	11/20/23-18:31	ROV container	3050	SP=10m, GL=80m, PW=40m
8	11/20/23-21:03	11/18/23-21:13	ROV container	3050	SP=10m, GL=80m, PW=40m
8	11/20/23-21:13	11/18/23-21:43	ROV container	3050	SP=5m, GL=40m, PW=20m

TW-COTDR

No.	Time (UTC)		Place	sensor depth (m)	remarks
	start	end			
7	11/19/23-18:36	11/20/23-19:03	ROV container	3050	AC=4096, Step=0.050 GHz
7	11/19/23-19:04	11/19/23-19:23	ROV container	3050	AC=8192, Step=0.10 GHz
8	11/20/23-18:36	11/18/23-19:21	ROV container	3050	AC=8192, Step=0.10 GHz

Table 5. List of the fiber optical sensing operation test.

2.5 Installation results

2.5.1 Orientation of the ROVplatform

Orientation of the ROV platform was estimated by checking an orientation of the Borehole/DONET interface by the ROV's camera. Figure 21 shows the orientation of the ROV platform in the C9038B observatory.

During the installation of the LTBMS, while the ROV platform was being assembled in the moonpool, the orientation of the painted frame of the borehole fiber-optic strainmeter corresponding to the position of the beginning of fiber winding was confirmed by the ROV's camera (Fig. 22). This enabled us to determine the relative relationship between the ROV platform and the position of the beginning of the fiber winding, and we confirmed that the direction of the beginning of the ROV winding was approximately in the southerly direction (183 degree, Fig. 23).

2.5.2 Borehole fiber optical strainmeter

As part of the LTBMS installation process, we repeatedly conducted operational tests to confirm the integrity of the optical fiber cable. This is because the fiber may be damaged by unexpected vibrations of the drill pipe during installation or by strong contact with the hole wall while descending into the hole.

Fig. 23 shows the results of the borehole fiber optical strainmeter operation test during installation of the LTBMS. The noise of the strain data decreased as the borehole

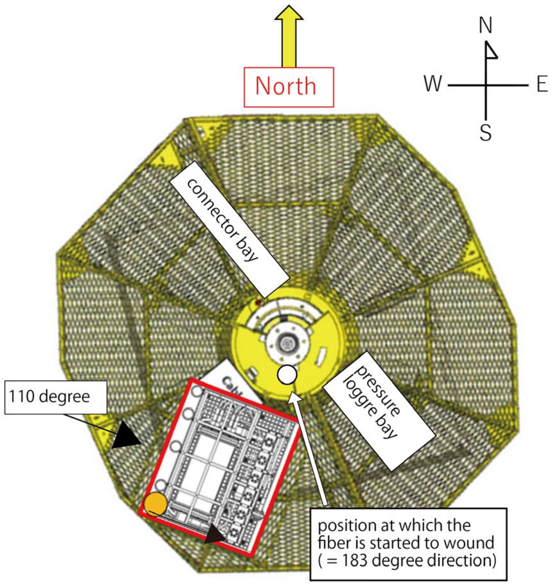

Fig. 21. Orientation of the ROV platform and the position at which the fiber is started to wound.

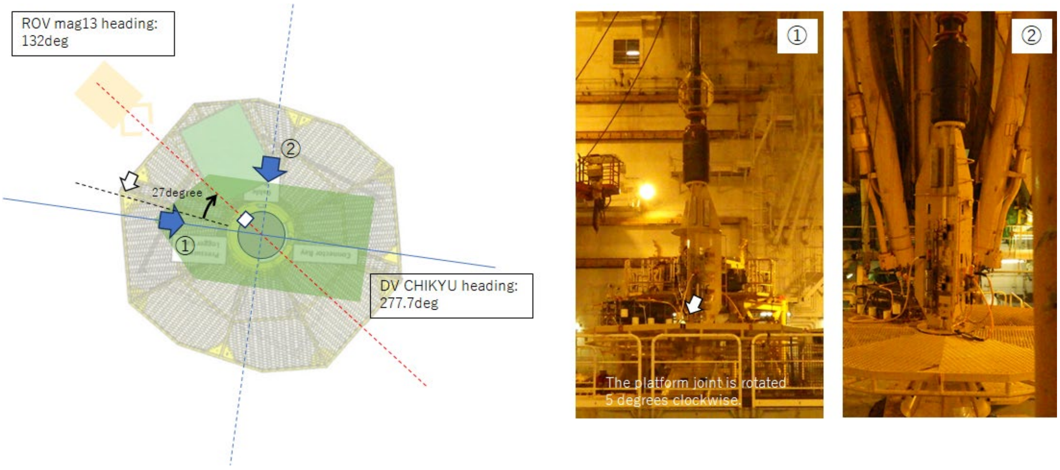

Fig. 22. Positional relationship between the ROV platform and the start of fiber winding.

fiber optical strainmeter was lowered into the borehole. When the CORKhead landed on the wellhead, the noise level became very low. It can be seen that the noise level became even lower after cementing was performed and the drill pipe was separated from the CORKhead. The measurements were taken approximately 1-2 hours after cementing had finished, and the cement had not yet hardened in the borehole. Therefore, it is assumed that the main cause for the reduction in the noise level was that the drill pipe separation. By connecting CORKhead to a drill pipe, it may be possible to capture ocean vibrations through the

borehole strain win_ch_base 4500		
AD	4500-4509	
HK	452A, 452C, 452D, 452E	
SF	4540-4547	
UN	4570-4579, 4584, 4585, 4590, 4591, 4594, 4596, 4597	
borehole pressure gauge		
P0	4550	SN157228
P1	4551	SN157229
P2	4552	SN157230
T0	4553	SN157228
T1	4554	SN157229
T2	4555	SN157230
thermistor		
1	4556	
2	4557	

Table 6. Channel list of the LTBMS data

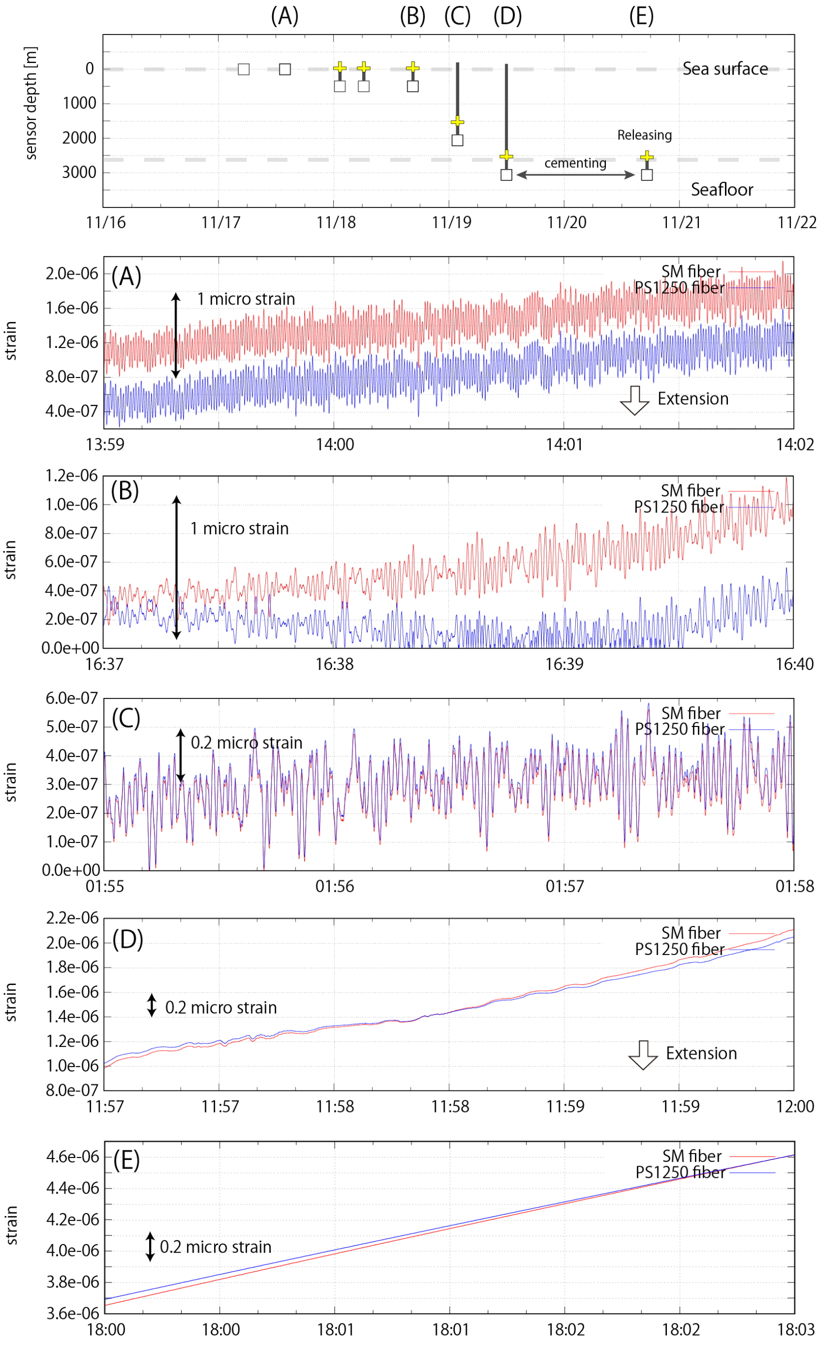

Fig. 23, Result of borehole fiber optical strainmeter operation test during installing the LTBMS. Top most figure shows status of the installation. The figures below show the data when indicated by A-E in the top most figure.

casing pipe.

Fig. 24 shows a comparison of noise spectrum of the borehole fiber optical strainmeter during measurements of Test #5, #6, and #7. Test #5 was conducted when the CORK head and the ROV platform were on board, and showed a noise with a peak at 4-6 seconds, which was likely caused by the movement of the ship. Test #7 was conducted after the CORK head landed on the wellhead, and compared to Test #5, the

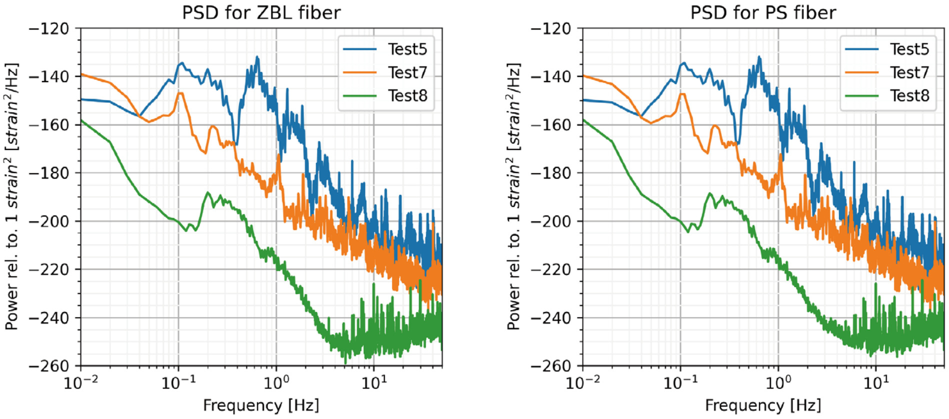

Fig. 24, Noise spectrum of the borehole fiber optical strainmeter for the test 5, 7, and 8. Left and right figure shows the result of the single mode fiber (ZBL) and PS1250 fiber, respectively.

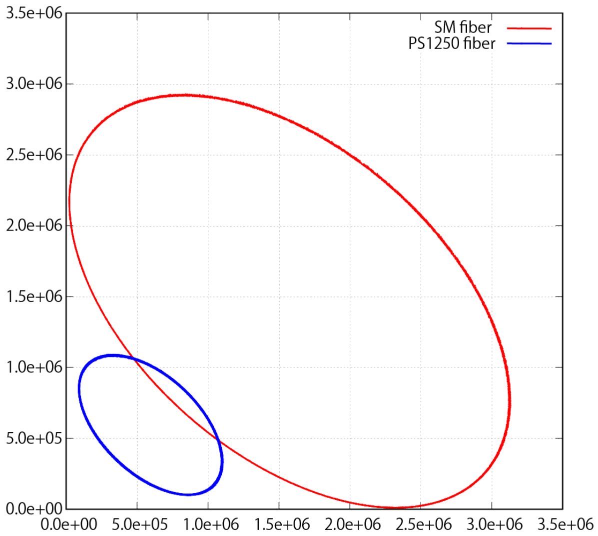

Fig. 25, Interference ellipse results of the borehole fiber optical strainmeter for the test 8. Red and blue ellipse show the results of the single mode fiber and the PS1250 fiber, respectively.

noise level decreased by about 20-30 dB from 1 second to 10 seconds. Test #8 has a noise level that is about 20 dB lower than the result of Test #5, and a signal that seems to be microseis can be clearly seen especially around 6-8 seconds. These results indicate that the optical fiber cable can be observed even after the LTBMS is installed. These results are also supported by the fact that the interference ellipse shown in Fig. 25 can be clearly seen. The initial test results of the fiber optic strainmeter are extremely promising and we expect to collect high resolution strain data once the LTBMS is connect to the DONET network.

2.5.3 Fiber optic sensing

Fig. 24 shows the spatiotemporal distribution of strain rate measured by DAS. The amplitudes of the 1st cable are the largest and are saturated (Fig. 26a and 26c) since the 1st cable was swung by ship motion, due to ocean swell. Sections 4480-4930 m and 5780–6230 m show similar spatiotemporal variation (Fig. 26b), indicating that these sections correspond to the forward and returned sections of the borehole fiber cable. The amplitudes of these sections are ~1000 nstrain/s. The characteristic of these sections is propagating waves from the upper to the lower of the drilling pipe. The period and velocity are ~8 s and ~6 km/s, respectively (Fig. 27). The period is similar to that of swells of the ocean, and the velocity is also similar to that of the elastic wave speed of steel (~5.6 km/s). Therefore, these waves are considered to be caused by ship motions propagated through the pipe.

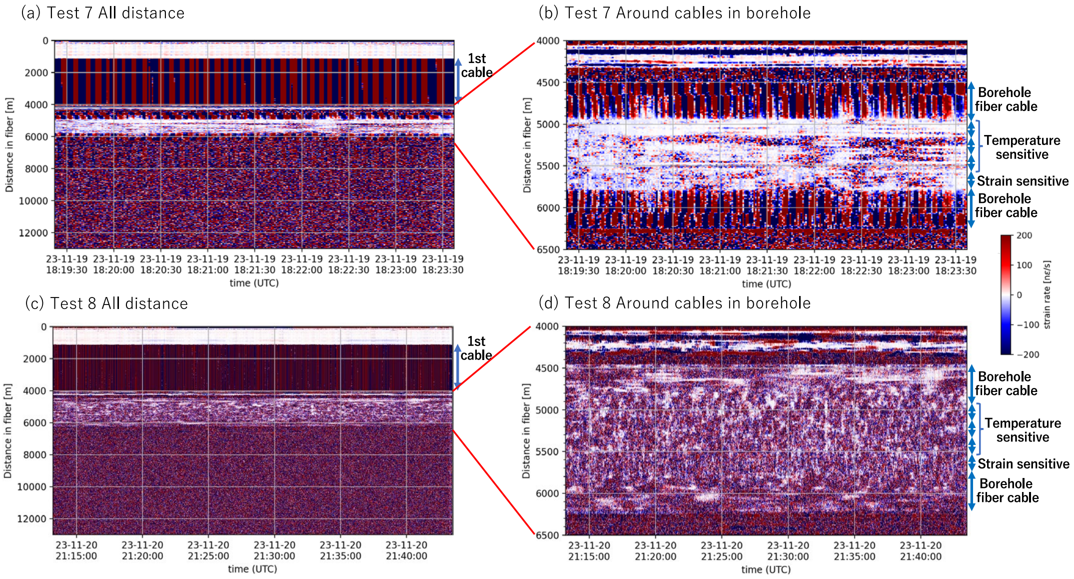

Fig. 26, Spatiotemporal distribution of strain rate amplitudes in (a) all distances of Test 7, (b) 4000–6500 m of Test 7, (c) all distances of Test 8, and (d) 4000–6500 m of Test 8.

The propagating waves are discontinuous bordering on 4650 m, which corresponds to the boundary between the casing and open hole. The part of 4930–5780 m corresponds to cables of sensing section of the borehole fiber optical strainmeter (800 m). In this section, propagating waves are not confirmed such as that in the Fig. 24b. For the Test #8, no waves were observed to propagate in all sections. The difference between Test #7 and #8 is that the

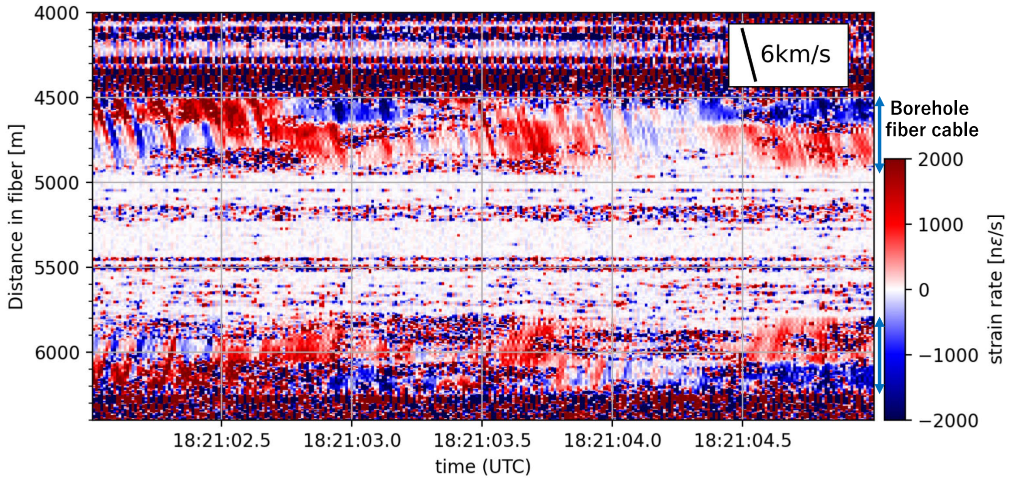

Fig. 27, Zoom up of spatiotemporal distribution of 4000–6500 m of Test 7.

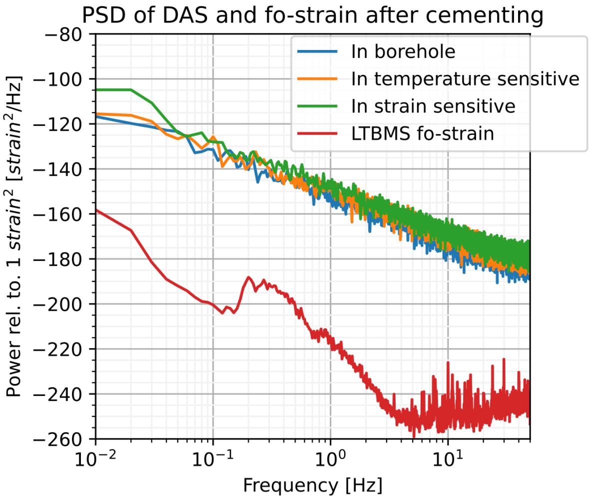

Fig.28, Comparison of the noise spectrum between the DAS and borehole fiber optical strainmeter after cementing.

borehole was cemented and the drill pipe above the CORKhead was disconnected.

To compare detectability between fiber optic borehole strainmeter in the LTBMS and DAS, we calculated the power spectral density by averaging the 100-s power spectral densities with 10-s overlapping using Welch's method (Fig. 28, Welch, 1967). The fiber optic strainmeter showed significantly better detectability than DAS. A peak of microseisms can be observed for fiber optic strainmeter between 0.1 – 1 Hz, however, the noise floor for DAS was too large to observe the peak of the microseisms. The difference between the fiber optic strainmeter and DAS was approximately 40 dB.

For TW-COTDR measurement, several trials were carried out to measure differences in strain and/or temperature conditions between the cementing process (Fig. 29). However, the following two difficulties were clarified for TW-COTDR measurement on the ship. The first one is an effect of connectors. Slip-rings and connectors which are used for optical fiber

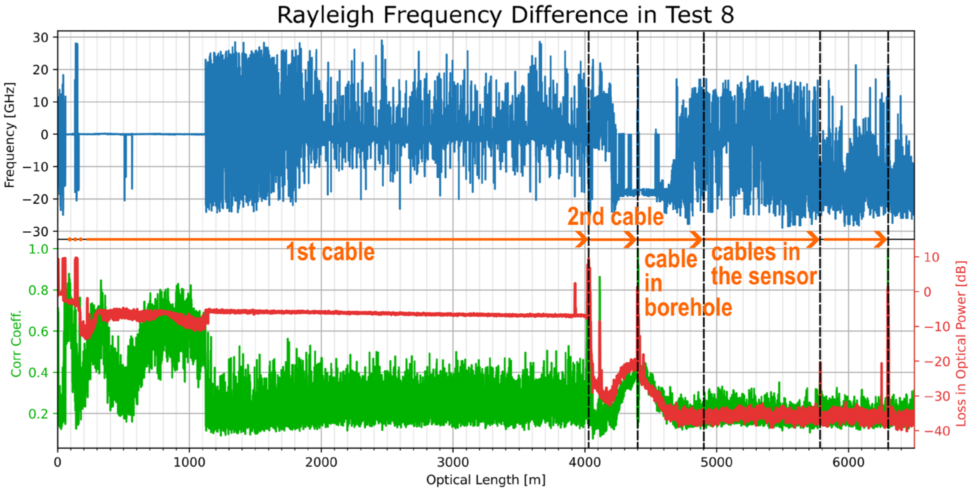

Fig. 29, Frequency differences and correlation coefficients between two measurements in Test 8. Blue, green, and red lines show the frequency difference, the correlation coefficient, and loss in optical power of TW-COTDR measurement, respectively.

in ROV are reflective type. Thus, large amounts of reflection and loss occurred at the connectors in contrast to the use of non-reflective connectors for optical sensing (4000 m and 4400 m in Fig. 29). The other cause is a rapid variation in strain relative to sampling interval of TW-COTDR of 10 minutes. During the 10 minutes approximately 30 GHz of frequency difference is expected based on strain record by fiber optic strainmeter. That is almost the same width as scanning range of a measurement. Therefore, spectral shapes are not highly correlated.

2.5.4 Pore-fluid pressure measurement

During the installation process, the PSU was tested twice (Test #7 and #8) via an ROV connection which supplied 24V power to the LTBMS interface and allowed for communication with the PSU. Pressure data was collected before (Test #7) and after cementing (Test #8), with approximately 26 hours between tests (Fig. 30).

During test 7, the valves on the CORK head were in the "CLOSED" and "OCEAN" positions. All three pressure transducers within the PSU measured the hydrostatic pressure at the seafloor (Fig. 30). For test #8, the valve positions were "CLOSED" and "ZONE" which enabled measurement of the formation by pressure transducers P1 and P2 while P0 continued to measure seafloor pressure (Fig. 30). The pressure data collected during installation had a high noise level compared to tests #4-6. The seafloor pressure transducer (P0) had a noise level of approximately 500 hPa and the two formation pressure transducers (P1 and P2) had a noise level of approximately 1500 hPa. However, it is possible that the source of the high noise is the ROV electrical connection. When the LTBMS interface is connected to the DONET network in the coming months, it is plausible that the noise will substantially reduce.

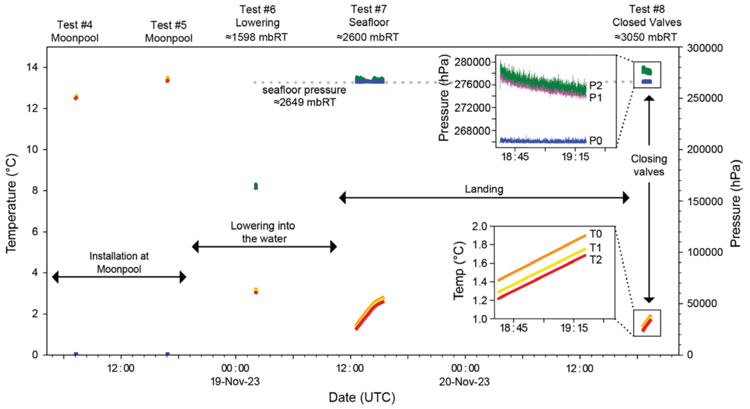

Fig. 30, Pressure and temperature record of the pore-fluid pressure gauge during a series of operation check. T0, T1 and T2 show a seafloor temperature recorded by the three pressure transducers. P0 is a seafloor pressure. P1 and P2 are the pressure at the bottom of the pressure ports (see Fig.1).

3 Coring and shear strength evaluation at DN2G-1 site

3.1 Coring

Coring was operated at Site C9039 (see cruise information chapter). All cores were taken by the Hydraulic Piston Coring System (HPCS) of the *Chikyu*. The HPCS is designed to take a 9.5-m long core. Cores were then used for shipboard sampling and analysis. General core analysis flow is shown in Fig. 31, and detailed protocol is described in the Method chapter.

Cores retrieved on the deck were delivered to the Core Cutting Area generally about 30 minutes later after the retrieval. The recovered core length excluding lengths of obvious void spaces were then measured and the Drilling Operations team determined the penetration length (= advance) based on the drilling parameters, the recovered core length and the core condition. A core was cut into 1.4-m long sections and each section length was entered into the J-CORES database, along with core identification information, drilling advance and depth information. Unconfined strength (UCS) measurements were performed at the bottom of the section by the penetrometer. Then each core sections were examined with the X-ray Computed Tomography (X-CT) scanner. After the X-CT scanning, core sections were examined by the whole-round multisensory core logger (MSCL-W) for gamma ray attenuation (GRA) density, P-wave velocity (V_P), Noncontact electrical resistivity (NCR), magnetic susceptibility (MS), and natural gamma radiation (NGR). Measurement intervals are described in the Method. After the MSCL-W scanning, thermal conductivity measurements and personal samplings were conducted for the whole-round cores. Then the core section was split lengthwise along the lines delimiting the archive and working halves. Archive-half sections were designed for nondestructive image measurements using Tri-sensor core logger (TSCL). For working-half sections, shipboard analysis of physical properties was conducted; shear strength and UCS measurements for half-round core, and discrete samples were taken for moisture and density (MAD) measurements. All half-round core sections were vacuum sealed and transferred to cold storage. After expedition, all cores were transported to the Kochi Core Center (KCC) in Kochi, Japan.

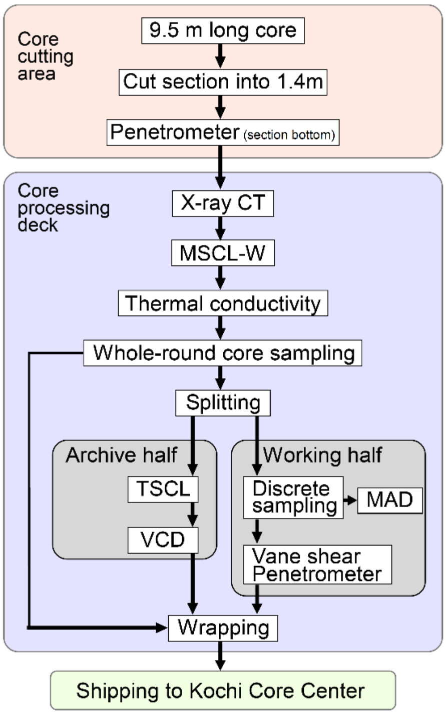

Fig. 31. Core processing and measurement flow for the Hole C9039A. X-CT = X-ray computed tomography, MSCL-W = whole-round multisensor core logger, TSCL = Tri-sensor core logger, VCD = Visual core description, MAD = moisture and density.

3.2 Method

3.2.1 X-ray computed tomography (X-ray CT)

X-ray CT scanning for preliminary assessment was done immediately after dividing the core into 1.4 m sections. Whole-round-core (WRC) sections were screened to avoid drilling disturbance and to take typical lithology. X-ray CT images will be also used to identify 3-D sedimentary and structural features to infer lithology in intervals where visual core description will not be possible because core had been taken as WRC samples for personal sampling.

Our methods followed those in the measurement manual prepared by CDEX (X-ray CT Scanning, Version 3.00; 24 March 2015) and used during previous IODP expeditions (e.g., IODP Expedition 370). The X-ray CT instrument on the Chikyu is a Discovery CT 750HD (GE Medical Systems) capable of generating thirty-two 0.625 mm thick slice images every 0. 4 s, the time for one revolution of the X-ray source around the sample. Data generated for each core consist of core-axis-normal planes of X-ray attenuation values with dimensions of 512 × 512 pixels. Data were stored on the server as Digital Imaging and Communication in

Medicine (DICOM) formatted files. The DICOM files were restructured to create 3-D images for further investigation.

X-ray intensity varies as a function of X-ray path length and the linear attenuation coefficient (LAC), μ, of the target material. LAC is a physical index about the X-ray beam reduction during translation of target materials. LAC is led from the relationship between physical properties of target materials (i.e., chemical composition, density, and state). The basic measure of attenuation, or radiodensity, is the CT number given in Hounsfield units (HU):

CT number = $[(\mu_t - \mu_w)/\mu_w] \times 1000$,

where μ_t is LAC for the target material, and μ_w is LAC for water. The distribution of attenuation values mapped to an individual slice comprises the raw data that are used for subsequent image processing. Successive 2-D slices yield a representation of attenuation values in 3-D pixels referred to as voxels. Analytical standards were air (CT number = −1000), water (CT number = 0), and aluminum (2477 < CT number < 2487) in an acrylic core mock-up.

3.2.2 Whole-round multisensory core logger (MSCL-W)

MSCL-W is a complex of sensors for measuring physical properties. Whole-round samples were measured for gamma ray attenuation (GRA) density, *P*-wave velocity (V_P), magnetic susceptibility (MS), Noncontact electrical resistivity (NCR), and natural gamma radiation (NGR) by the MSCL-W (Geotek, Ltd., London, United Kingdom) after X-ray CT scan completed and thermally equilibrated at room temperature for approximately 4 hours.

Gamma ray attenuation density (GRA)

GRA is based on the detection of a gamma ray beam during its passage through the sediment. The beam, produced by a 370 MBq 137Cs gamma ray source within a lead shield with a 5 mm collimator, was directed through the whole-round core samples. The gamma ray detector includes a scintillator and an integral photomultiplier tube to record the gamma rays that pass through the cores. GRA bulk density (ρ_b) was calculated as

$$\rho_b = \ln(I_0/I)/\mu d,$$

where I_0 is gamma ray source intensity, I is measured intensity of gamma rays passing through the sample, μ is Compton attenuation coefficient, and d is sample diameter, respectively. Since the Compton attenuation coefficient (μ) and source intensity (I_0) can be treated as constants, ρ_b is calculated from I. The gamma ray detector was calibrated with a sealed calibration core, which is a standard core liner filled with distilled water and aluminum cylinders (2.7 g/cm^3) with six different diameters of 1 to 6 cm. GRA density measurements on core samples were conducted every 4 cm for 4 s. The spatial resolution is 5 mm.

***P*-wave velocity (V_P)**

P-wave (compressional) velocity (V_P) is defined by the time required for a compressional wave to travel a set distance:

$$V_P = d/t_{\mathrm{core}},$$

where d is the path length of the wave across the core, and t_{core} is the travel time through the core. V_P transducers on the MSCL-W system measure total travel time of the compressional wave between transducers. The system is mounted horizontally on the MSCL-W system and measures d and t_{core} perpendicular to the core axis. The total travel time observed is composed of t_{delay} (time delay related to transducer faces and electronic circuitry), t_{pulse} (delay related to the peak detection procedure), t_{liner} (transit time through the core liner), and t_{core} (travel time through the sediment or rock). The system is calibrated using a core liner filled with distilled water, which provides control for t_{delay}, t_{pulse}, and t_{liner}.

With these calibrations, core velocity (V_P) can be calculated on whole-round specimens in core liners as follows:

$$V_P = (d_{cl} - 2d_{liner})/(t_o - t_{pulse} - t_{delay} - 2t_{liner}) = (d_{cl} - 2d_{liner})/(t_o - t_w - (d_{cl} - 2d_{liner})/V_w),$$

where d_{cl} is outer diameter of the core liner, d_{liner} is liner wall thickness, t_o is measured total travel time, t_w is measured travel time through the water-filled calibration liner, and V_w is known V_P of pure water at room temperature. The above equation assumes that the core completely fills the core liner. The measurement interval of V_P is 4 cm, and the V_P source frequency is 230kHz

Noncontact electrical resistivity (NCR)

Bulk electrical resistivity is controlled by solid grain resistivity, interstitial water resistivity, pore space distribution, and pore connectivity. The noncontact resistivity sensor on the MSCL-W system induces a high-frequency magnetic field in the core with a transmitter coil. This generates an electrical current in the bulk sediment that is inversely proportional to its resistivity. The secondary magnetic field generated by this induced electrical current is measured by a receiver coil. Electrical resistivity (ρ) is defined by the electrical resistance and geometry of the core measured:

$$\rho = R(A/L)$$

where R is electrical resistance, L is the length of measurement, and A is cross-sectional area of the core. To measure the smaller magnetic field accurately in order to evaluate the induced current, a differencing technique has been developed that compares readings from the sample core to readings from an identical set of coils operating in air. Electrical resistivity data were obtained at 2 cm intervals on the MSCL-W.

Magnetic susceptibility (MS)

MS is the degree to which a material can be magnetized by an external magnetic field. An 8 cm diameter Bartington loop sensor was used to measure MS. An oscillator circuit in the sensor produces a low-intensity (~80 A/m root-mean-square) nonsaturating alternating magnetic field (0.565 kHz). This pulse frequency was converted into MS. The spatial resolution of the loop sensor is 23–27 mm and the measurements were conducted at every 4 cm along the core.

Natural gamma radiation (NGR)

The core samples were monitored for NGR emissions to obtain spatial variability in radioactivity. NG R measurement employs lead-shielded counters optically coupled to a photomultiplier tube and connected to a bias base that supplies high-voltage power and a signal preamplifier. Two horizontal and two vertical sensors are mounted in a lead cube-shaped housing. The NGR system records radioactive decay of ^{40}K, ^{232}Th, and ^{238}U. Measurements were conducted every 16 cm with a count time of 30 s, and the resolution is 120–170 mm in terms of core length. Background radiation noise was determined by taking measurements on a water-filled calibration core. Two radioactive isotope standards (^{133}Ba and ^{60}Co) were used for energy calibration and adjustment of the spectral detection windows.

3.2.3 Thermal conductivity measurements

Thermal conductivity was measured on sediment and rock samples using the full-space needle probe (Von Herzen and Maxwell, 1959). The needle probe was inserted into WRCs through a hole drilled in the core liner. The full-space measurements produce a scalar thermal conductivity value in the plane perpendicular to the orientation of the probe.

The measurements were conducted after the cores had equilibrated to room temperature (i.e., ~24°C). At the beginning of each measurement, temperature in the core was monitored to ensure that thermal drift was <0.4 m°C/min (within 2 min). After the confirmation of the temperature equilibrium, a calibrated heat source was applied and the change in temperature was recorded for ~80 s. Values of thermal conductivity were based on the observed rise in temperature for a given quantity of heat. The full-space needle probes were calibrated at least once every 24 h. The calibration was performed on Macor samples of known thermal conductivity (1.611 ± 2% W/[m·K] and 1.652 ± 2% W/[m·K]).

3.2.4 Tri-sensor core logger (TSCL)

TSCL consists of a photo image logger, color spectroscopy, and electrical resistivity meter. In this expedition, only the first two were conducted since electrical resistivity was measured using MSCL-W. TSCL was performed on the archival half of the core after the core was cut into halves via whole-round sampling. Digital images of archive-half cores were acquired by a line-scan camera (SW-4000T-MCL: 3 CMOS prism line scan camera, JAI). Digital photographs were taken under two different Gamma correction settings (0.45 and 1.0). The equivalent color data can provide information on relative changes in bulk material composition that are useful to analyze stratigraphic correlation and lithologic characteristics and cyclicity. The color spectrophotometer (MetaVue™ VS3200, X-Rite) was used to measure color reflectance of split core sections (archive half). The measurement intervals of reflectance spectrophotometry were 4 cm, and the measurement height from the sample surface was 4 mm. The reflected light is collected in the color spectrophotometer's integration sphere and divided into wavelengths at 10 nm pitch (400–700 nm). The color spectrum is then normalized by the source light of the reflectance and calibrated with the measurement of a pure white standard. The calibration of the spectrophotometer was conducted once a day, followed by the adjustments of the white balance of the camera and the lighting condition. The condition of the sensors was checked by measuring a color reference (ColorChecker Classic Mini, Calibrite) and diffuse reflectance standards (white and gray Spectralons, Labsphere). The measurements of the ColorChecker and the two Spectralons were carried out after the calibration and before each core measurement. The measured color spectrum is normally converted to lightness (L*) and chromaticity variables a* and b*. The L* value represents lightness, from black (L* = 0) to white (L* = 100). The a* value represents color changing from pure green (a* = −127) to pure red (a* = 127), and the b* value represents color changing from pure yellow (b* = −127) to pure blue (b* = 127).

3.2.5 Visual core description (VCD)

VCD was carried out on the archive halves of each core. Detailed observations of each section were initially recorded by hand on paper, adjacent to the printed scanned image of that section. Site, hole, core, section and depth (in centimeters core depth below seafloor) are given at the right top of the VCD sheet. Columns on the VCD sheets include the graphic representation, drilling (coring) disturbance, sedimentary structures, and color. Cores were logged by section, and the information from VCD forms was converted to core-scale plots. Since some section was missing due to WRC sampling, X-ray CT images and lithologic description of whole-round sample residues were used for compliments. Provisional lithological name for each lithology was decided from quick determination of the grain size. Drilling disturbances, if any, are documented with its type and classification: Flow-in, Fall-in, Soupy, Cracked, and Slightly – Moderately – Heavily. The dominant sediment colors are recorded in section description on the VCD sheets using color codes (the corresponding hue and chroma) and names in Revised Standard Soil Color Charts.

3.2.6 Shear strength and UCS measurements

Undrained shear strength and UCS were measured using a semi-automated laboratory vane shear device (Model WF23500) and a penetrometer (Model E-284B) on the working-half core. Vane shear and penetrometer measurements were made at discrete about two and three locations per section on the working-half samples. In general, measurements were made adjacent to MAD sampling locations. Care was taken to conduct tests within undisturbed and homogeneous parts of the core. To minimize disturbance effects resulting from the MAD sampling, shear measurements were generally conducted first, followed by

MAD sampling.

Vane shear measurements

Vane shear measurements were made with the vane rotation axis. The vane shear strength of sediments $Su(v)$ [kPa] is calculated as:

$$Su(v) = T / K_v,$$

where T (N-m) is the torque required to fail the material and K_v (m^3) is a constant depending on the dimensions of the vane (Blum, 1997). The vane height and diameter were set as 12.7 mm for all measurements. Failure torque was determined by measuring the degrees of rotation of a spring (Spring-1, 2, and 4 used onboard the Chikyu), and a linear calibration equation for each spring and vane size relating the rotation angle to torque. Vane shear results were generally considered reliable for shear strength values less than approximately 150 to 200 kPa, which is the strength range without excessive cracking and separation.

Penetrometer measurements

The penetrometer provides a measure of unconfined compressive strength (UCS) of sediment samples. The UCS is calculated by dividing the penetration resistance generated by pushing a cylindrical probe into the core surface to a 6.5 mm penetration depth by the area of the penetration probe (Blum, 1997). All measurements in this expedition were conducted using a probe with a nominal diameter of 6.35 mm (0.25 inches). The UCS values were calculated from the average of three penetration trials conducted at adjacent points on the core. Typical spatial separation between trials was on the order of 1 cm. The unit was converted from kg/cm^2 to kPa by the following equation;

$$\text{UCS [kPa]} = \text{UCS [kg/cm}^2\text{]} \times 9.81 \times 10.$$

The undrained shear strength $Su(v)$ [kPa] corresponds to the UCS [kPa] value dividing by 2.

3.2.7 Moisture and density measurements (MAD)

Discrete samples from working-half cores were used for determination of index properties (bulk density, grain density, dry density, water content, porosity, and void ratio). Index properties were determined from phase relations, mass measurements on wet and dry specimens, volume measurements on dry specimens, and corrections for salinity. In general, one discrete sample (~10 cm^3) was collected from each core section using a cylinder. Sample intervals were adjusted to obtain minimally disturbed homogeneous samples.

Wet and dry masses were measured using a paired electronic balance system, which is designed to compensate for ship heave. A standard mass of similar value to the sample was placed on the reference balance to increase accuracy. The sample mass was determined to a precision of ±0.005 g. The balance system was calibrated at least once per 24 h.

To minimize desiccation, MAD sample collection was immediately followed by measurement of wet sediment mass (M_{wet}). After M_{wet} measurements, samples were dried in a convection oven at 105° ± 5°C for 24 h. Dry samples were placed in a desiccator for at least 1 h to equilibrate to room temperature (~24°C), and then dry sediment mass (M_{dry}) and dry sediment volume (V_{dry}) were measured. A five-chamber Quantachrome pentapycnometer was used to measure V_{dry} with a helium-displacement technique providing precision of ±0.04 cm^3. The five-chamber system allowed the measurement of four sample volumes and one calibration sphere. Each measured volume is the average of five measurements. The calibration sphere was rotated between all measurement chambers to monitor for errors in each chamber. The pycnometer was calibrated at least once per 24 h.

Standard ODP/IODP practices were used to determine pore water mass and volume, salt mass and volume, and solid grain mass and volume (Blum, 1997). From these data, bulk density, dry density, grain density, porosity, and void ratio were calculated (Blum, 1997) as described below. Standard seawater density (1.024 g/cm3), salinity (35 parts per thousand [ppt]), and a constant salt density (2.22 g/cm3) were assumed for all calculations.

Water content

Water content (W_c) was determined following the American Society for Testing and Materials (ASTM) standard D2216 (ASTM International, 1990). Corrections are required for marine samples containing sea water. In addition to the water content calculation in ASTM D2216 (i.e., the ratio of pore fluid mass to dry sediment mass; W_c[dry]), we also calculated the ratio of pore fluid mass to total sample mass (W_c[wet]). The equations for water content are

$$W_c(\mathrm{dry}) = (M_{\mathrm{wet}} - M_d)/(M_d - sM_{\mathrm{wet}}),$$

and

$$W_c(\mathrm{wet}) = (M_{\mathrm{wet}} - M_d)/M_{\mathrm{wet}}(1 - s),$$

where M_{wet} is total mass of the discrete sample, M_d is mass of the dry sample, and s is salinity assumed as 0.035, respectively.

Bulk density

Bulk density is the density of a discrete core sample ($\rho_b = M_{\mathrm{wet}}/V_t$) including both of solid grains and pore water. Total wet sample mass (M_{wet}) was measured immediately after collecting each discrete sample using the dual-balance system. Total sample volume assuming 100% saturation ($V_t = V_g + V_{pw}$) was determined from the pycnometer measurement of grain volume (V_g) and the calculated volume of pore water (V_{pw}). Solid grain and pore water volume were determined as

$$V_g = V_d - (M_{\mathrm{wet}} - M_d)s/\rho_{\mathrm{salt}}(1 - s),$$

and

$$V_{pw} = (M_{\mathrm{wet}} - M_d)/\rho_{sw}(1 - s),$$

where V_d is dry volume, ρ_{salt} is salt density, and ρ_{sw} is standard seawater density, respectively.

Porosity and void ratio

Porosity (ϕ) relates the volume of the pores to total sample volume; void ratio (e) relates the pore volume to solid grain volume. They are calculated from the water content and the bulk density as

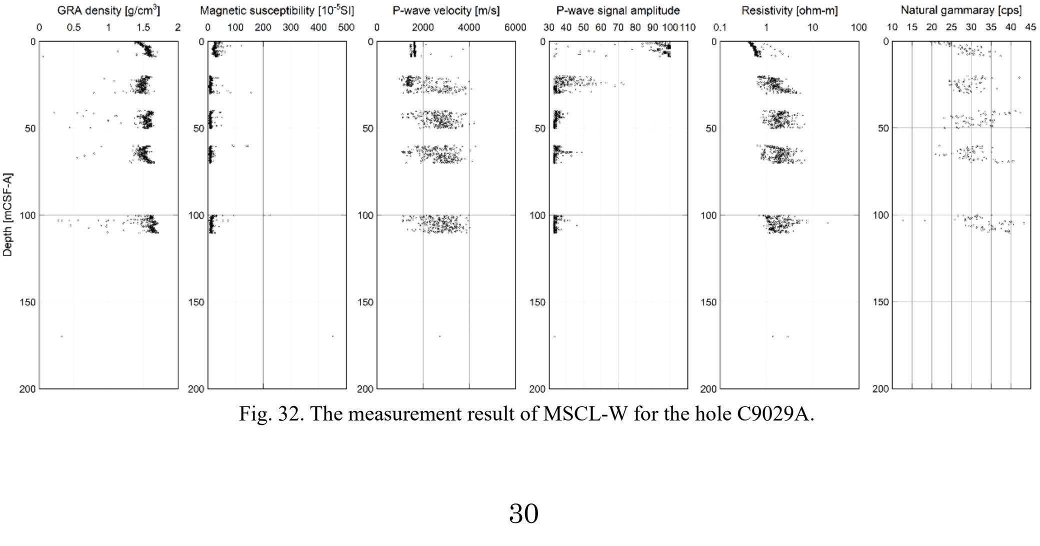

Fig. 32. The measurement result of MSCL-W for the hole C9029A.

$\phi = \rho_b V_{pw}/M_{wet}$,
and
$e = V_{pw}/V_g$.

3.3 Results

3.3.1 MSCL-W

The measurement result of MSCL-W is summarized in Fig. 32. MSCL-W measurements were performed on all cores recovered. A sharp increase in gamma-ray density was observed from just below the seafloor, increasing to approximately 1.7 at the bottom of the Core 1 (~9.5 m). Subsequent depths show a slight upward trend, with a baseline of about 1.6 g/cm^3, and the density reaches 1.7 g/m^3 in the Core 6 (Fig. 32A). P-wave velocities of sufficient quality are limited to the Core 1 (Figure 2xxD and E). These nondestructive geophysical results can be attributed to cracks in the core structure, especially those caused by degassing. Due to the insufficient length of the Core 6 (0.24 m), the number of data for each measurement was small and no natural gammaray measurements were recorded (Fig. 32F).

3.3.2 Thermal conductivity measurements

Thermal conductivity measurements were not possible for most parts of the acquired cores due to cracking caused by gas expansion. Thermal conductivity measurements were made for only two homogeneous, unstructured portions of the cores. The results of the

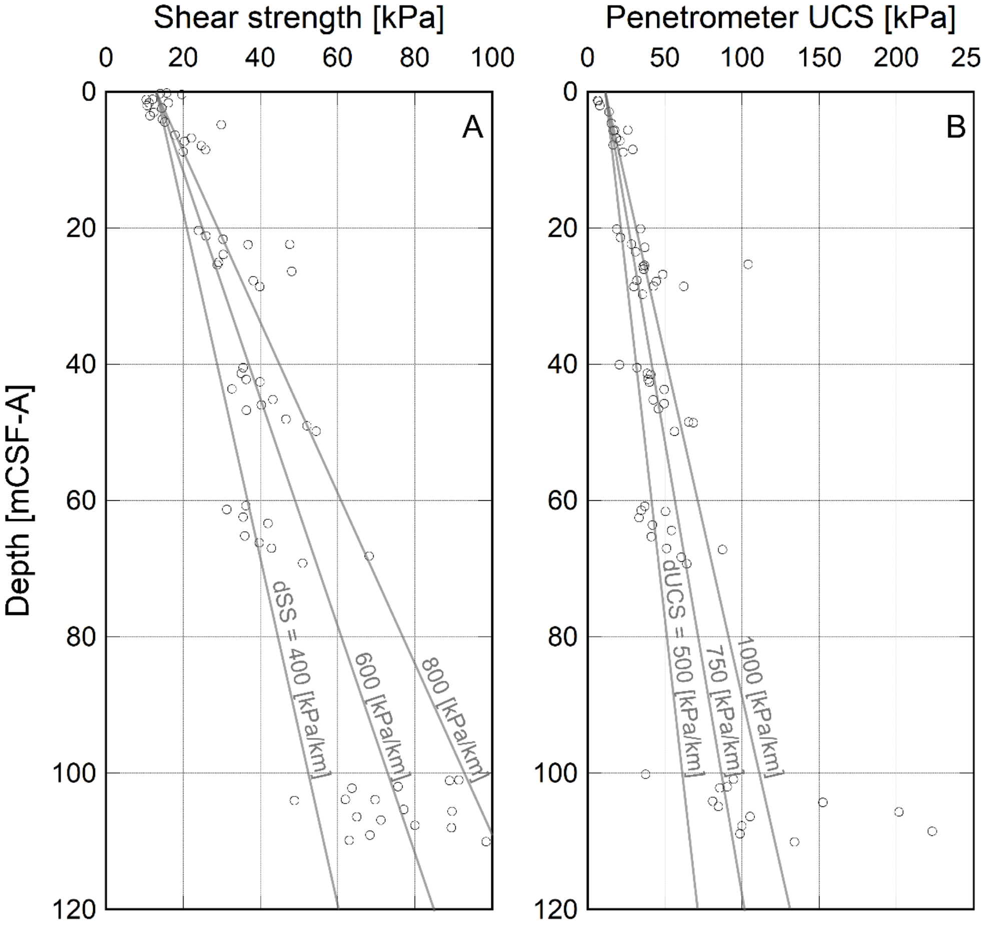

Fig. 33. The result of strength measurements using vane shear (a) and penetrometer (b). Lines in each column indicate the gradient of strength by depth.

measurements together with the standard are summarized in Table 7.

3.3.3 Shear strength and UCS measurements

The downhole profiles of vane shear and penetration tests are shown in Fig. 33. Vane shear measurements were made at one or two locations per section on the working half, whereas penetrometer UCS measurements were conducted on both of WRC (section top/bottom) and working-half. Care was taken to conduct tests within undisturbed and homogeneous parts of the core. To minimize disturbance effects resulting from the MAD sampling, strength measurements were generally conducted first, followed by MAD sampling. Measuring locations and the values of strength are summarized in Table 8 and 9.

3.3.4 MAD

The MAD data obtained from 60 samples of Hole C9039A are provided in Fig. 34 and Table 10. For the MAD measurements, one or two samples were taken per section. Lithologies representative of the section were selected. After sampling, weighing and dry volume measurements were made according to the procedures described in the Method. Sediment bulk densities display the general pattern of downhole increase from 1.4 g/cm^3 at the seafloor to ~1.8 g/cm^3 by 100 mbsf. Grain densities indicate approximately constant within 2.8–3.0 g/cm^3, higher values than a quartz grain. Porosity displays a downhole decrease from 78% at seafloor to ~60% by 100 mbsf.

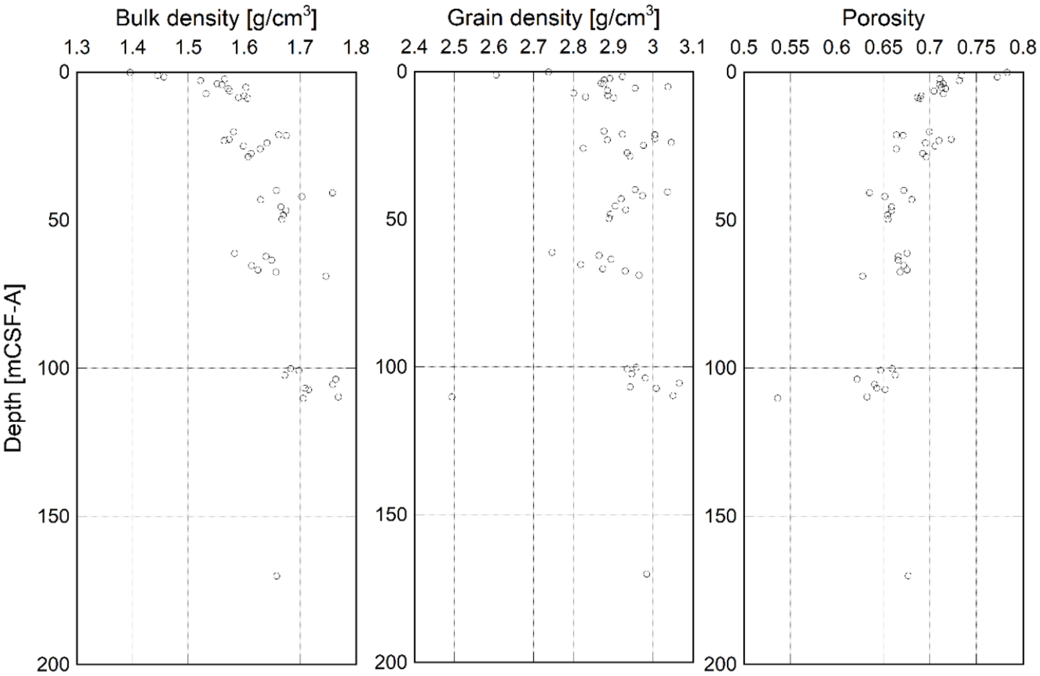

Fig. 34. The result of moisture and density measurements.

Depth [m CSF-A]	Shear strength [kPa]
0.2	15.73
0.25	14.06
0.375	19.6
1.1	12.05
1.15	10.42
1.61	16.1
1.66	11.14
2.01	10.59
2.41	14.44
3.015	12.33
3.515	11.42
4.015	14.62
4.435	15.2
4.825	29.89
6.35	17.84
6.795	22.06
7.275	20.3
7.915	24.7
8.545	25.75
8.795	19.95
20.36	23.92
21.16	25.93
21.665	30.29
22.415	47.55
22.435	36.75
23.885	30.36
25.06	29.12
25.395	28.78
26.365	48.04
27.735	38.11
28.605	39.8
40.47	35.56
41.315	35
42.19	36.31
42.56	39.87
43.615	32.57
45.175	43.24
45.945	40.25
46.71	36.35
48.04	46.62
49.005	52.05
49.8	54.48
60.73	36.24
61.33	31.25
62.41	35.53
63.335	41.93
65.175	35.94
66.19	39.68
66.99	42.87
68.135	68.16
69.18	50.92
101.01	91.38
101.09	88.96
101.955	75.57
102.195	63.66
103.82	61.99
103.9	69.69
104.005	48.79
105.31	77.07
105.58	89.59
106.41	64.94
106.885	71.14
107.635	80
108.025	89.46
109.075	68.29
109.825	62.97
110.04	98.42

Table 8. Shear strength at Hole C9039A

Depth [m CSF-A]	UCS [kPa]	Sand
1.29	6.54	
1.41	6.87	
2.01	8.01	
2.95	13.9	
4.655	15.37	
5.625	17.49	
5.625	26.16	
5.715	16.68	
6.825	18.64	
7.195	20.93	
7.795	16.68	
8.463	29.27	
8.885	22.89	
20.105	34.34	
20.18	18.8	
21.395	21.26	
22.375	28.45	
22.83	37.11	
23.49	30.9	
25.33	103.99	○
25.49	36.79	
25.655	35.97	
26.055	36.3	
26.805	48.72	
27.675	31.88	
27.825	44.47	
28.52	42.67	
28.565	62.29	○
28.63	30.08	
29.75	35.64	
40.055	20.6	
40.495	31.88	
41.345	38.75	
41.48	40.88	
42.223	39.24	
42.595	40.06	
43.685	49.54	
45.22	42.51	
45.76	49.54	
46.53	45.78	
48.48	65.4	
48.605	68.51	
49.845	56.24	
60.8	37.11	
61.395	34.66	
61.565	50.52	
62.5	33.35	
63.59	42.02	
64.375	54.28	
65.285	41.2	
67.03	51.18	
67.185	87.31	
68.295	60.82	
69.255	64.26	
100.13	37.61	
100.855	94.5	
101.995	90.42	
102.165	85.67	
104.1	80.93	
104.29	152.38	
104.88	84.69	
105.695	201.6	
106.355	105.13	
107.715	99.9	
108.505	223.18	
108.865	98.59	
110.075	133.91	

Table 9. Penetrometer UCS at Hole C9039A

Depth [m CSF-A]	Bulk density [g/cm^3]	Grain density [g/cm^3]	Porosity
0.16	1.3956	2.7372	0.7831
1.21	1.445	2.6054	0.7338
1.7	1.4564	2.9227	0.7723
2.41	1.565	2.8909	0.7102
2.91	1.5215	2.877	0.7315
4.04	1.5517	2.8696	0.7141
4.31	1.5599	2.8758	0.7106
5.2	1.6027	3.0372	0.7125
5.67	1.571	2.9544	0.7167
6.43	1.5738	2.8849	0.7045
7.36	1.5313	2.8004	0.7144
8.05	1.6002	2.8861	0.6906
8.63	1.5901	2.83	0.6865
8.93	1.606	2.9007	0.6899
20.21	1.5809	2.8765	0.6994
21.24	1.662	2.9232	0.6641
21.46	1.6753	3.0045	0.6711
22.72	1.5729	3.0048	0.7229
23.2	1.5641	2.8851	0.7098
23.98	1.6404	3.0455	0.6951
24.98	1.5985	2.9753	0.7056
25.99	1.6288	2.8248	0.6641
27.56	1.6123	2.9348	0.6921
28.65	1.6071	2.9418	0.696
40.01	1.6577	2.9545	0.6717
40.84	1.7582	3.0361	0.6351
42.03	1.7031	2.9733	0.6516
43.17	1.6294	2.9193	0.6806
45.54	1.6657	2.9048	0.6588
46.81	1.6748	2.9307	0.6587
48.35	1.6698	2.8921	0.6543
49.72	1.6676	2.8887	0.6548
61.19	1.5828	2.7457	0.6754
62.26	1.6388	2.8641	0.6659
63.54	1.649	2.8943	0.6658
65.36	1.613	2.8184	0.6717
66.85	1.6245	2.8732	0.6753
67.56	1.6569	2.9299	0.6679
68.97	1.7465	2.9642	0.6276
100.16	1.6829	2.958	0.6593
100.78	1.6981	2.9348	0.6472
102.35	1.6723	2.9465	0.6628
103.75	1.764	2.9799	0.6217
105.5	1.7583	3.0658	0.6404
106.74	1.7092	2.9422	0.6428
107.25	1.715	3.0082	0.6518
109.67	1.7686	3.0502	0.6325
110.16	1.7054	2.494	0.5364
170.12	1.6578	2.9837	0.6766

Table 10. Moisture and density at Hole C9039A

3.3.5 Drilling parameters

Drilling parameters were recorded as time-based data every second. The drilling data were compiled into csv files on a daily basis and include the measurements shown in Table 11. Fig.35 - 37 show typical drilling parameters converted to depth from the rig floor for each borehole. Note the differences in the drilling assemblies used for each hole. In particular, casing was installed from 0-50 mbsf and 0-100 mbsf in holes C9038A and C9038B, respectively, and intermittent HPCS coring was performed up to 100 mbsf in hole C9039A (see Operation chapter). The ROP in all holes is approximately 100 m/hour with large variations, C9038B is drilled at a relatively constant rotational speed and pump flow rate, and the input parameters that significantly affect the drilling rate are constant below 2720 mBRT, except for WOB. In hole C3039A, coring was conducted at the point where the ROP was zero. The piston core is penetrated for 8.5 m or 9.5 m from these points, which means that the drillers will drill around the edges of the core, but the torque values are comparable to the other sections where the center bit was placed.

Measurements	Unit
Date(UTC)_Time(Zone)	-
Weight_on_Hook(Traveling_block)	[kN]
Weight_on_Hook(Deadline)	[kN]
Choke/Kill_A_Pressure	[MPa]
Tensioner_Load	[kN]
Present_Bit_Position	[m]
Total_Measured_Depth	[m]
Rate_of_Penetration_(ROP)	[m/h]
Hook_Height	[m]
Heave_Movement	[m]
Weight_on_Hook(Selected)	[kN]
Weight_on_Bit	[kN]
Top_Drive_Torque	[kNm]
Top_Drive_RPM	[RPM]
Stand_Pipe_Pressure1	[MPa]
Stand_Pipe_Pressure2	[MPa]
Stroke_per_Minutes_#1	[SPM]
Stroke_per_Minutes_#2	[SPM]
Stroke_per_Minutes_#3	[SPM]
Stroke_per_Minutes_#4(future)	[SPM]
Stroke_per_Minutes(Total)	[SPM]
Pumps_Flow_Rate	[l/min]
Flow_out_as_%	[%]
Total_Pits_Volume	[m^3]
Pits_Volume_gain/loss	[m^3]
CMT_A_Pressure	[MPa]
CMT_B_Pressure	[MPa]
Boost_Pressure	[MPa]
CMC_cylinder_stroke	[m]

Table 11. List of drilling parameters

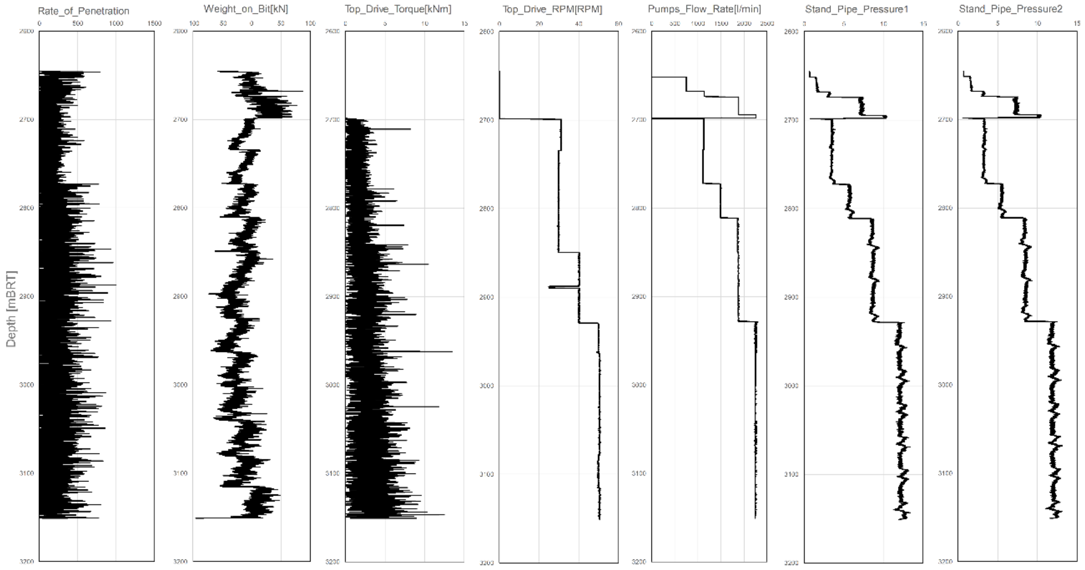

Fig. 35. Examples of recorded drilling parameter while drilling at C9038A.

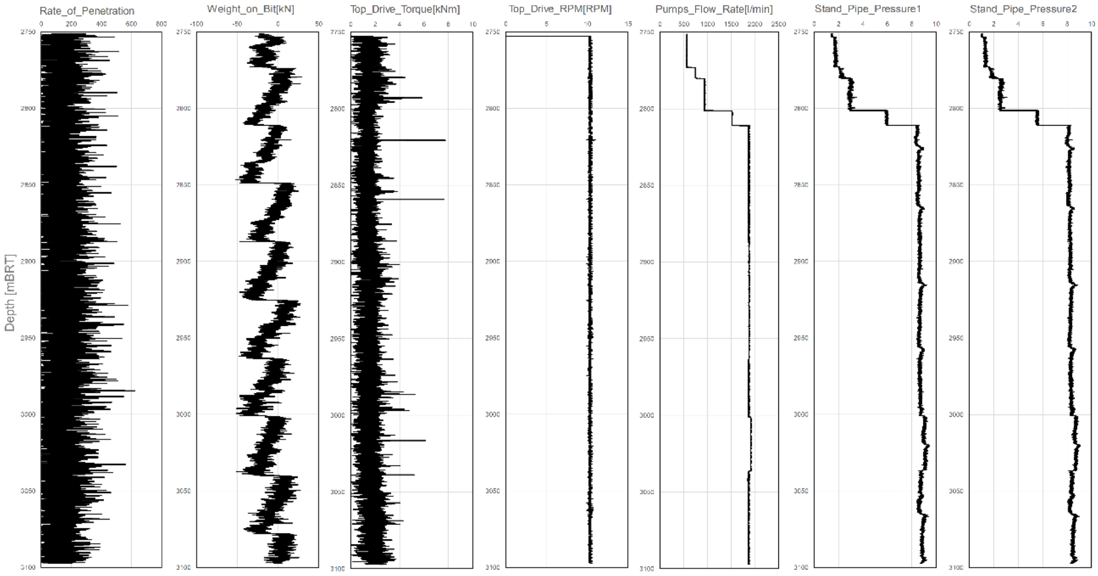

Fig. 36. Examples of recorded drilling parameter at C9038B.

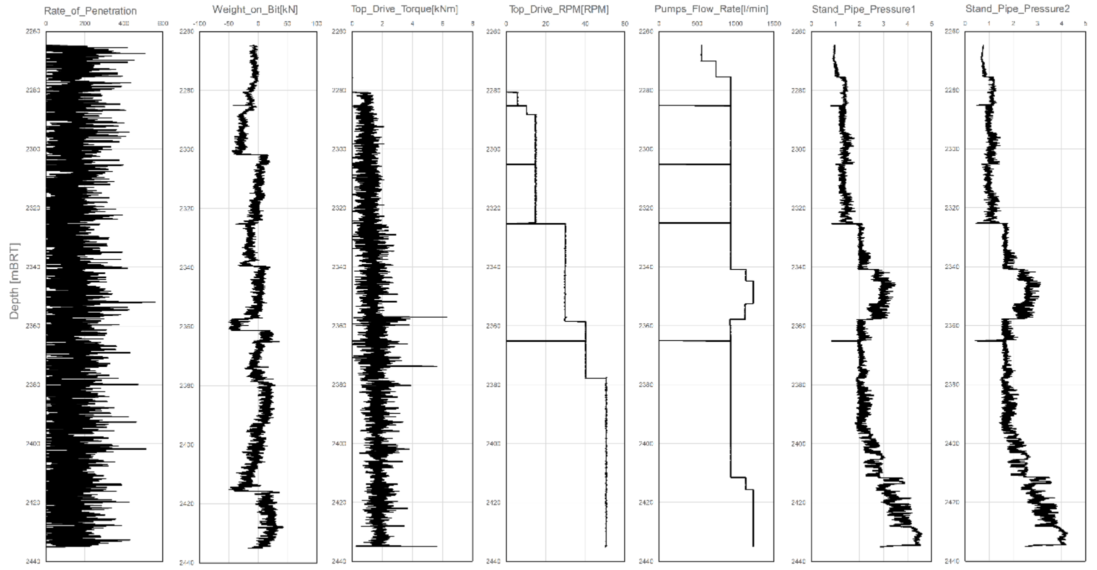

Fig. 37. Examples of recorded drilling parameter at C9039A.

3.3.6 Comparison of strength by various methods

Before this cruise, the seismic wave velocity structures at the drilling site were obtained by a prior seismic reflection survey. The velocity structure provides a depth profile of V_p near the drilling sites (Fig. 38a). The profile at DN2F-1 (corresponding to site C9038) is extracted from the KIN038 survey data obtained by the KM18-10 cruise. Since the seismic data was processed twice by DUG, first at the time of the cruise and then in 2023, both velocity profiles are shown as DN2F-1_old and DNF-1_new, respectively. For DN2G-1, the drill site was extracted from the Muroto 3D-MCS data. The depth profile of density was also estimated along with the respective velocity profiles and is summarized in Fig. 38b. At DN2F-1, despite the same data at the same location, differences in estimated velocity structure can be seen. DNF-1_new shows a relatively monotonic increase, with velocities 80 - 100 m/sec slower than DN2F-1_old up to around 400 mbsf. DN2F-1_old shows a velocity reversal around 300 mbsf. On the other hand, site DN2G-1 (corresponding to site C9039) shows a complex velocity structure, with a velocity of 1500 m/s similar to that of seawater up to 150 mbsf, increasing rapidly to 1800 m/s at around 300 mbsf. The velocity continues to increase monotonically at depths below 300 mbsf, showing a higher V_p than that of Site C9038. The density shows a similar trend to that of V_p.

Based on the V_p estimated by the seismic reflection survey, we calculated the strength profile for the two sites (three curves) using empirical equations that converts the V_p to UCS (Chang et al. 2006). The empirical

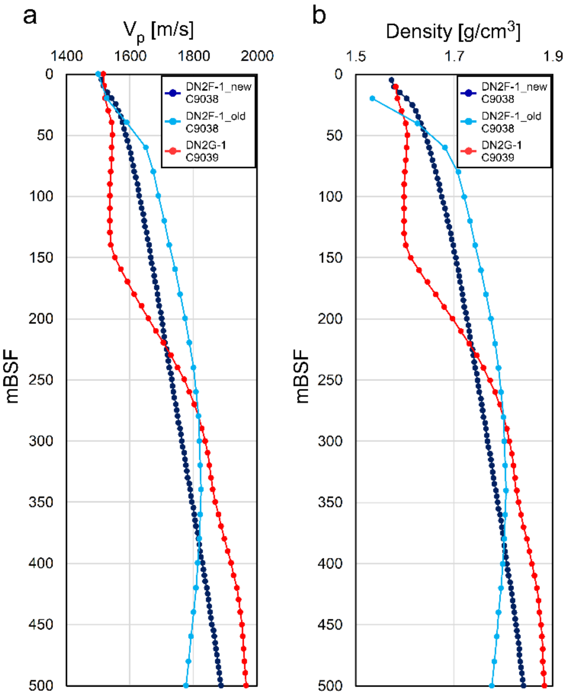

Fig. 38. Depth profiles of P-wave velocity (a) and density (b) estimated from seismic reflection survey.

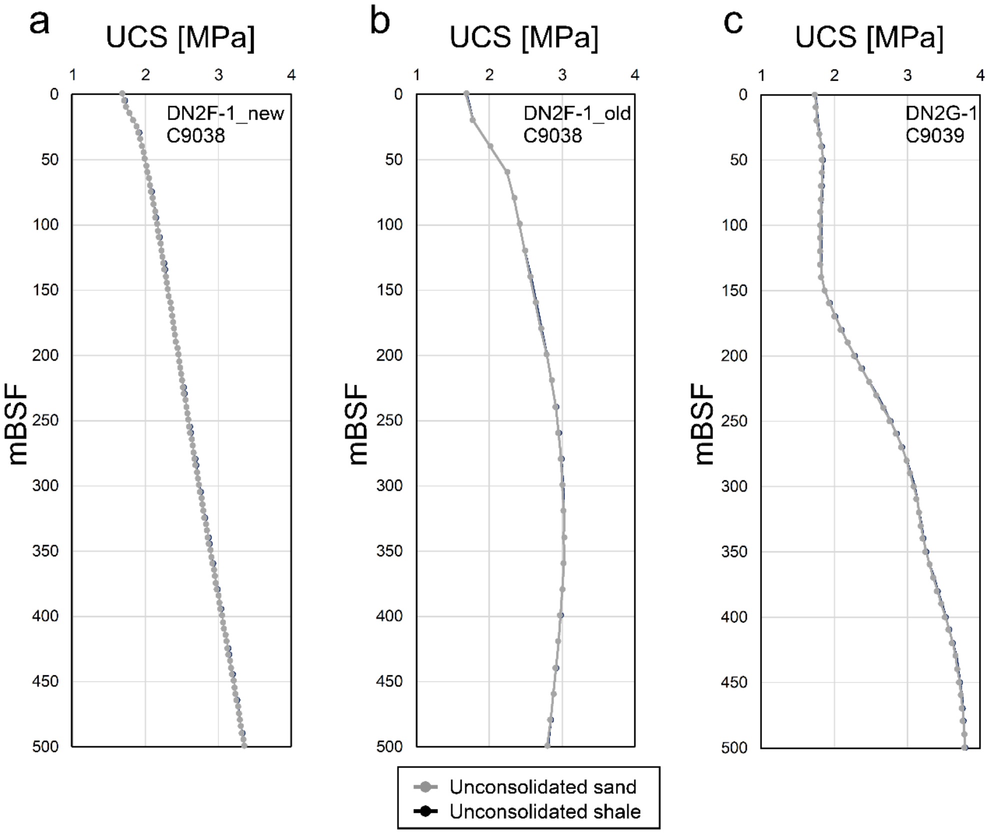

Fig. 39. Depth profiles of UCS for (a): DN2F-1_new, (b): DN2F-1_old, and (c): DN2G-1.

equations were developed for the Gulf Coast, unconsolidated sandstone:

$$\mathrm{UCS} = 1.4138 \times 10^{7} \times [1000000/(3.281\times V_p)]^{-3},$$

and for unconsolidated shale:

$$0.5\ (304.8\ /\ [1000000/(3.281\times V_p)])^{3}$$

.

The depth profile of the UCS calculated by the above is shown in Fig. 39. The three UCS profiles at two sites show similar profiles to V_p. In all cases, the UCS values were on the order of MPa, and the UCS of site C9038 tended to be higher than that of C9039.

The density estimated by the seismic reflection survey was also compared to density measurements using cores collected during this cruise and previous drilling projects. Samples from sites C0002, C0006, and C0018 drilled during the NanTro SEIZE project were used for comparison. The depth profiles of all densities are summarized in Fig. 40. The colored dots connected by lines in the figure are the densities estimated from seismic reflection surveys. The density distribution estimated by the prior survey is in good agreement with the density of the core sample taken at C9039A. It also shows reasonable agreement with the data from sites C0002 and C0018. However, the density reduction in the 50-200 mbsf of the seismic-density (red line + dot) is not seen in the core density (red dot). The strength profile of Hole C9039A shown in Fig. 33 was also compared with the strength distribution of boreholes drilled along the Nankai Trough (Fig. 41). The results show that both penetrometer UCS and vane shear strengths of the samples from Hole C9039A are comparable to those of Holes C0002B/D and C0018A in terms of strength and depth increase rate. On the other hand, the sample strength at Hole C0006E/F was significantly lower than that at Hole C9039A, from ~40 mbsf. In any case, the values of these strengths were more than an order of magnitude lower than those estimated from the sonic

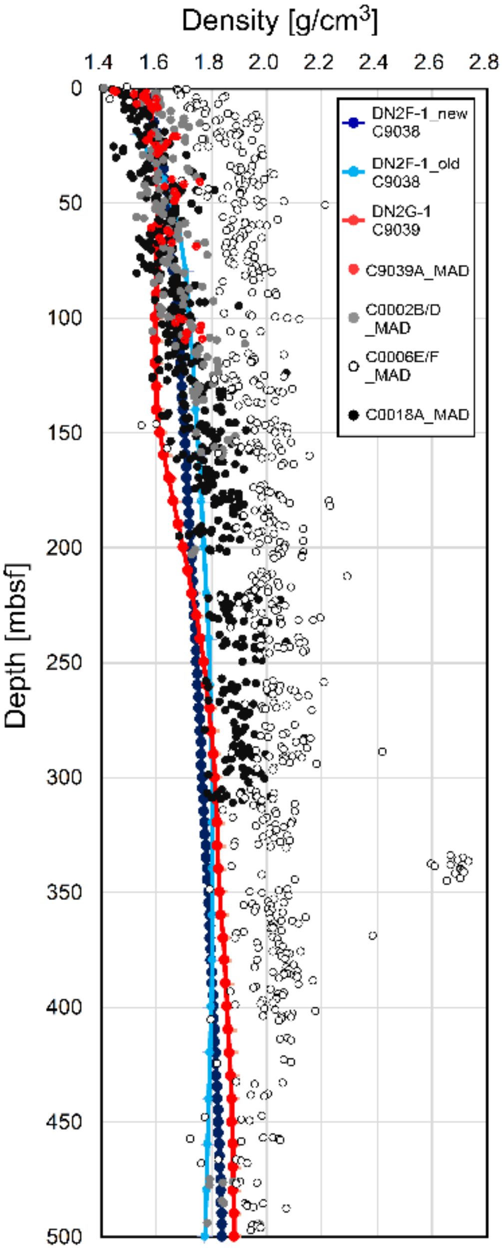

Fig. 40.Summarized density profiles from seismic surveys and core samples.

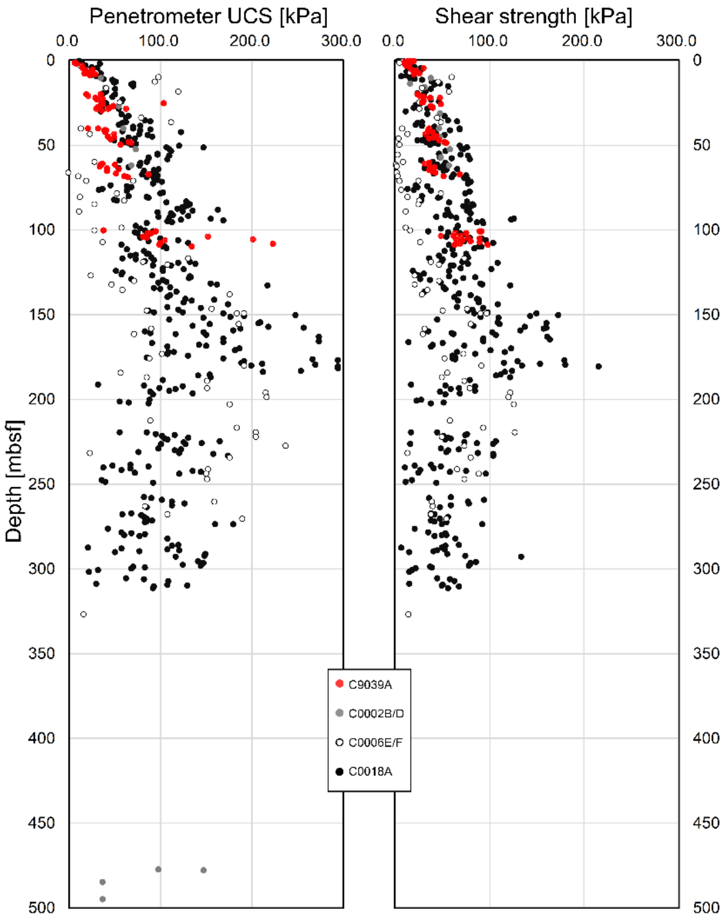

Fig. 41.Summarized strength profiles from core samples.

velocities at sites C9038 and C9039 (Fig. 39). It is difficult to directly compare these two methods, suggesting that strength testing of surface cores is a direct method for obtaining strength profiles near the subseafloor.

4 Future plans

We confirmed that the LTBMS sensors work correctly during the CK23-03 cruise via a series of operation test. In January 2024, we are going to connect the DN2F-1 observatory to the DONET cable network. This will enable us to monitor seismicity in a real-time, and contribute to understanding the actual situation of slow slip occurrences in the Nankai trough.

5 Cruise log

Date	Time		Operation / Activity descriptions
	From	To	
11/06/2023	00:00	07:00	Stand-by at Shimizu port.
	07:00	24:00	Sail to Site ND2F-1.
11/07/2023	00:00	09:00	Continue to sail to Site NDF-1. Arrive at Site NDF-1 at 08:18.

	09:00	12:45	Prepare ROV dive. Field arrival check. Prepare for running 20”CSG.
	12:45	18:30	Conduct ROV test dive.
	18:30	24:00	Deploy transponders by ROV. Make up and run 20”CSG
11/08/2023	00:00	01:30	Continue to deploy transponders by ROV.
	01:30	05:00	Conduct DP calibration and field arrival check
	05:00	08:00	Resume making up and running 20” CSG
	08:00	10:30	Lower and secure 20”CSG with HART to the moonpool cart. Remove HART
	10:30	14:30	Make up 10-5/8” jetting BHA and insert into 20”CSG. Make up HART.
	14:30	19:00	Run 20”CSG with jetting BHA to 1400 mBRT. Meanwhile conduct DAS test, pressure test with 6 MPa on hydraulic lines for the primary and secondary CORK heads, respectively.
	18:30	19:00	Rig service for hydraulic elevator hoses.
	19:00	24:00	Resume running 20”CSG to 2540 mBRT. Dive ROV with hotstab for HART and manual torque tool for secondary unlock. Check the bit rotation by ROV.
11/09/2023	00:00	02:00	Continue to run 20”CSG with jetting BHA to 2651 mBRT. Meanwhile confirm the hole location with the chief scientist. Tag seabed (water depth: 2651.0 mBRT) Space out string for jetting operation and fill up string. Sput-in Hole C9038A at 02:08. Coordinates: 32°52.1365'N, 135°18.1634'E
	02:00	04:30	Conduct jetting 20”CSG from 2651.0 to 2699.3 mBRT.
	04:30	0800	Keep 20”CSG at the present position until formation recovered.
	08:00	08:15	Conduct slump tests and confirm 20”CSG stability (1880 kN and 1790 kN for 5 min, respectively). Height of the wellhead: 5 m above seafloor.
	08:15	09:00	Release 20”CSG by hydraulic activated running tool (HART).
	09:00	17:15	Pull out the jetting BHA with HART to surface.
	17:15	24:00	Prepare HART for the next run. Conduct Rotating Guide Roller (RGR) function test. Set up for pumping PROTECTZONE.
11/10/2023	00:00	15:00	Make up and run in hole 10-5/8” motor drilling BHA to 2596 mBRT.
	15:00	15:30	Re-entry the 10-5/8” motor drilling BHA to Hole 9038A at 15:30.
	15:30	17:00	Wash down to 2699.0 mBRT (48.0 mbsf).
	17:00	24:00	Drill down from 2699.0 to 2879.0 mBRT (48.0 – 22.0 mbsf).
11/11/2023	00:00	09:30	Continue to drill down from 2879.0 to 3151.0 mBRT (228.0 – 500 mbsf). Reached TD: 09:35
	09:30	10:00	Circulation and bottoms up with sweeping out 10 m^3 SWG two times with 600 gpm x 10.0-13.1 MPa.
	10:00	12:15	Wiper trip from 3151.0 to 2687.0 mBRT (500 – 36.0 mbsf).
	12:15	15:45	Wiper trip from 2687.0 to 3147.0 mBRT (36.0 – 496 mbsf).
	15:45	17:30	Wiper trip from 3111.0 to 3147.0 mBRT (460 – 496 mbsf). Found taking weight 60 – 90 kN at 3146.5 mBRT and 3146.0 mBRT (495.5 – 495 mbsf). Suspected bottom hole filled by cuttings. Reciprocate string and pump with 10 m^3 SWG x 2 times with 700 gpm x 16.3 MPa, 30 rpm x 0-1.5 kN.

	17:30	19:30	Spot PROTECTZONE from CMT unit at 3146.0 mBRT (495 mbsf). Pull out the 10-5/8” motor drilling BHA from 3146.0 to 3108.0 mBRT (495 – 457 mbsf).
	19:30	20:30	Pull out the 10-5/8” motor drilling BHA from 3108.0 to 3046.0 mBRT (457 – 395 mbsf). Spot 20 m^3 SWG with 600 gpm x 13.5 MPa, 10 rpm x 1.0 kN.
	20:30	24:00	Pull out the 10-5/8” motor drilling BHA from 3046.0 to 2115.0 mBRT. Found the wellhead sank below the seafloor by ROV. Decided to make a new hole.
11/12/2023	00:00	07:00	Continue to pull out the 10-5/8” motor drilling BHA to surface.
	07:00	11:15	Prepare for jetting the next hole.
	11:15	18:15	Make up inner string BHA.
	18:15	20:15	Prepare for running 20”CSG.
	20:15	24:00	Make up and run 20”CSG.
11/13/2023	00:00	11:15	Continue to make up and run 20”CSG.
	11:15	15:00	Pick up and make up wellhead housing joint. Lower and secure 20”CSG with wellhead clamp and sling at moon pool working cart.
	15:00	17:30	Make up 10-5/8” jetting BHA.
	17:30	24:00	Run 20”CSG to 2403 mBRT.
11/14/2023	00:00	02:15	Continue to run 20”CSG to 2649 mBRT. Confirm coordination and tag on seafloor at 01:55 Water depth: 2649.0 mBRT (2620.5 mbsl)
	02:15	08:15	Spud-in Hole C9038B at 02:25 Coordinates: Lat: 32°52.1115'N, Long: 135°18.1652'E 20”CSG jetting from 2649.0 mBRT to 2751.3 mBRT (0 – 102.3 mbsf) Stick out: 6.5 m above seafloor.
	08:15	12:30	Keep 20”CSG at the present position until formation recovered.
	12:30	22:15	Conduct slump test at 260 kN and 360 kN for 10 min each. Confirm 20”CSG and wellhead is stable (stick out keeps 6.5 m above seafloor). Release HART and pull out the jetting BHA with HART to surface.
	22:15	24:00	Rig services Make up and run the 10-5/8” motor drilling BHA in hole.
11/15/2023	00:00	07:45	Continue to run the 10-5/8” motor drilling BHA to 2642 mBRT.
	07:45	09:30	Re-entry Hole C9038B at 07:54. Wash down to 2751.0 mBRT (102.3 mbsf).
	09:30	21:45	Drill down 10-5/8” hole from 2751.0 to 3149.0 mBRT (102.3 – 500 mbsf), with HPS: 10 rpm x 0.2-4.0 kNm, WOB: 0-40 kN, Auto ROP: 50 m/hr
	21:45	22:30	Circuration and bottoms up with sweeping 5 m^3 SWG x 2 times with 600 gpm x 8.9 MPa.
	22:30	24:00	Wiper trip from 3149.0 to 2728.0 mBRT (500 – 79 mbsf).
11/16/2023	00:00	02:00	Continue to wiper trip from 2780.0 to 3123.0 mBRT (29.0 – 474.0 mbsf).
	02:00	06:00	Wash down the 10-5/8” motor drilling BHA to 3147.5 mBRT (498.5 mbsf) with pumping 150 gpm x 1.7-2.4 MPa. Spot PROTECTZONE BP by CMTG pum and batch mixer at 3146.0 mBRT (497.0 mbsf). Pull out the 10-5/8” motor drilling BHA to 3046.0 mBRT (397 mbsf) and spot 22 m^3 SWG with 500 gpm x 7.1-7.8 MPa.
	06:00	15:00	Pull out the 10-5/8” motor drilling BHA to surface. Rig services.
	15:00	21:30	Make up HART with 6-m pony CORK head. Make up CMT stand and rack back in derrick. Rig up 4-1/2” TBG handling equipment.

			Prepare Moonpool.
	21:30	24:00	Run LTBMS completion to 29 mBRT. Meanwhile install mini-screen (Bottom) by SUS band.
11/17/2023	00:00	03:30	Continue to run LTBMS completion from 29 to 58 mBRT. Meanwhile install mini-screen (Bottom & Top) by SUS band arong 4-1/2” TBG. Make up and lower Sensor to Moonpool.
	03:30	08:00	Wait on weather.
	08:00	24:00	Resume to run LTBMS completion from 58 to 182 mBRT, while connecting sensor cables. 14:00-16:15 Conduct #1 sensor health check at 48 mBRT. 22:45-23:15 Conduct #2 sensor health check at 150 mBRT.
11/18/2023	00:00	21:45	Continue to run LTBMS completion from 182 to 488 mBRT, while connecting sensor cables. 10:00-10:45 Conduct #3 sensor health check at 476 mBRT. 15:00-16:30 Conduct #4 sensor health check at 485 mBRT.
	21:45	24:00	Install ROV platform.
11/19/2023	00:00	14:15	Continue to run LTBMS completion from 488 to 3108.5 mBRT. 00:00-02:30 Set and connect Interface Logger on ROV platform. Conduct #5 sensor health check at 486 mBRT. 03:30-06:00 Drift vessel to 50 m north from well center with 0.3 knot. 06:00 Resumet to run LTBMS completion. 10:30-11:30 Conduct #6 sensor health check at 2096 mBRT. 11:30-12:15 Adjust orientation of Interface Logger to west by ROV. 14:00-14:15 Confirm orientation of Interface Logger by ROV.
	14:15	19:45	Re-entry to Hole C9038B at 14:47. Circulation and bottoms up. Conduct slump test. Slack off 120 kN on wellhead and confirmed it keeps 6.5 m stick out height (no move). Land LTBMS completion at 16:39.
	19:45	24:00	Conduct #7 sensor health check (after landing to wellhead). Confirmed good communication with fiver optical strainmeter. Attempt to communicate with pressure logger.
11/20/2023	00:00	04:45	Continue to conduct #7 sensor health check. Observed noise on pressure logger, but acceptable (suspected nose comes from ROV interface). Confirmed good communication with DAS TWC OTDR.
	04:45	06:00	Conduct LTBMS cementing. Pump 10 m^3 of MUDPUSH II 05:30 ROV camera shut down suddenly.
	06:00	20:45	Recover ROV to repair. Cut and re-terminate ROV tether cable, conduct function test. Dive ROV to seafloor.
	20:45	23:30	Resume to conduct LTBMS cementing. Pump 5 m^3 of MUDPUSH II Pump 24.2 m^3 of FlexSTONE Pump 1.6 m3 of MUDPUSH II Displace 24.4 m^3 by pumping seawater
	23:30	24:00	Release HART. Slack off completion assembly 110 kN on wellhead for releasing HART. Attempt to stab in hotstab to HART by ROV.
11/21/2023	00:00	02:00	Continue to release HART. Pick up string and move vessel to 50 m downstream (270 deg) from the well while flushing string through CMTG pump.

	02:00	07:00	Change valve position by ROV: 2-way valve in “Close” and 3-way valve in “Zone.” Conduct #8 sensor health check. Confirm good communication with all sensors. Meanwhile pull the running BHA with HART out to 2300 mBRT.
	07:00	10:45	Continue to pull the running BHA with HART out from 2300 mBRT to surface, start layout the assembly and prepare for coring operation on drill floor. Meanwhile recover transponders by ROV.
	10:45	12:30	Recover ROV to surface.
	12:30	14:00	Stand-by for chopper operation.
	14:00	15:30	Remove ROV cursor rail. Prepare for sailing.
	15:30	20:00	Sail to Site DN2G-1 (Lat: 32°40.6777'N, Long: 134°29.9926'E).
	20:00	24:00	Set DPS mode Install ROV cursor rail Deploy transponders by ROV.
11/22/2023	00:00	04:45	Continue to deploy transponders by ROV. DP calibration and field arrival check.
	04:45	08:30	Move vessel to well center position. Meanwhile make up and run 10-5/8” HPCS coring BHA to 20 mBRT.
	08:30	15:15	Make up and run the 10-5/8” HPCS coring BHA to 2226.0 mBRT. Break circulation and check pressure. Meanwhile conduct seabed survey by ROV.
	15:15	16:00	Resume run the 10-5/8” HPCS coring BHA to 2260.0 mBRT. Run inner barrel for #1 HPCS core.
	16:00	16:30	Confirm coordination and water depth by tagging on seafloor by the BHA. Coordinates: 32°40.6777'N, 134°29.9926'E. Water depth :2265.0 mBRT (2236.5 mbsl)
	16:30	18:00	Spud in Hole C9039A at 16:39. Cut #1 HPCS core and recover the inner barrel. Wash down to 2280.0 mBRT (15.0 mbsf) and ream down to 2285.0 mBRT (20.0 mbsf).
	18:00	19:30	Run inner barrel for #2 core, cut #2 HPCS core, and recover the inner barrel. Ream down to 2300.0 mBRT (35.0 mbsf).
	19:30	20:45	Unload sinker bar and make connection. Run inner barrel for #3 core.
	20:45	22:30	Ream down to 2305.0 mBRT (40.0 mbsf). Cut #3 HPCS core and recover the inner barrel.
	22:30	23:30	Ream down to 2325.0 mBRT (60.0 mbsf). Run inner barrel for #4 core, cut #4 HPCS core, and recover the inner barrel.
	23:30	24:00	Unload sinker bar.
11/23/2023	00:00	02:15	Continue to unload sinker bar. Drop center bit. Drill down from 2325.0 to 2365.0 mBRT (60.0 – 100.0 mbsf) with auto ROP 35 – 60 m/hr. Sweep out 7 m^3.
	02:15	03:30	Load sinker bar and recover center bit.
	03:30	04:45	Run inner barrel for #5 core, cut #5 HPCS core and recover the inner barrel.
	04:45	05:15	Drop center bit and unload sinker bar.

	05:15	07:30	Drill down from 2365.0 to 2386.0 mBRT (100.0 – 121.0 mbsf) with auto ROP 50 m/hr.
	07:30	09:00	Load sinker bar and recover center bit.
	09:00	10:30	Run inner barrel for #6 core, cut #6 HPCS core and recover the inner barrel.
	10:30	17:30	Pull the 10-5/8” coring BHA out to surface. Meanwhile recover transponders by ROV, recover ROV and ROV cursor rail.
	17:30	24:00	Sail to Shimizu port.
11/24/2023	00:00	20:45	Continue to sail to Shimizu port.
	20:45	24:00	Stand-by off Shimizu port.
11/25/2023	00:00	08:15	Continue stand-by off Shimizu port.
	08:15	10:30	Move vessel to crew change point and conduct crew change by boat.
	10:30	24:00	Stand-by off Shimizu port.
11/26/2023	00:00	09:15	Continue stand-by off Shimizu port.
	09:15	10:30	Move vessel to crew change point and conduct crew change by boat.
	10:30	24:00	Stand-by off Shimizu port.
11/27/2023	00:00	13:45	Continue stand-by off Shimizu port.
	13:45	15:00	Sail and enter to Shimizu port.
	15:00	24:00	Stand-by at Shimizu port.
11/28/2023	End of cruise at 24:00		

6 References

Araki, E., Saffer, D. M., Kopf, A. J., Wallace, L. M., Kimura, T., Machida, Y., Ide, S., Davis, E. and IODP Expedition 365 shipboard scientists (2017),Recurring and triggered slow-slip events near the trench at the Nankai Trough subduction megathrust, Science, 356, 1157–1160.

Araki. E. et al., (2019), Observation of slow crustal deformation by seafloor fiber optic strainmeter connected to DONET seafloor cable observationnetwork, AGU Fall Meeting, San Francisco.

Ariyoshi, K., (2021a), Characteristics of Slow Slip Event in March 2020 Revealed From Borehole and DONET Observatories, Front Earth Sci8:600793. Doi:10.3389/feart.2020.600793.Ariyoshi, K., et al. (2021b), Precise Monitoring of Pore Pressure at Boreholes Around Nankai Trough Toward Early Detecting Crustal Deformation,Front Earth Sci 9:717696. Doi:10.3389/feart.2021.717696.

Baba, S., et al. (2020). Slow earthquakes illuminating interplate coupling heterogeneities in subduction zones. Geophysical Research Letters, 47,e2020GL088089.https://doi.org/10.1029/2020GL088089

Barnes P.M. et al. (2020). Slow slip source characterized by lithological and geometric heterogeneity, Science Advance, Vol 6, Issue 13, doi:10.1126/sciadv.aay3314.Hirose, T. (2021). High Fluid-Pressure Patches around the Source Regions of Slow Earthquakes along the Nankai Trough –A step forward tounderstand the generation mechanisms of slow earthquakes–, Press release of JAMSTEC.https://www.jamstec.go.jp/e/about/press_re-lease/20210617/

Kato A, et al., (2012). Propagation of slow slip leading up to the 2011 M(w) 9.0 Tohoku-Oki earthquake. Science. 2012 Feb 10;335(6069):705-8.doi:10.1126/science.1215141.

Machida, Y., et al. (2020). Mobile Pressure Calibrator for the Development of Submarine Geodetic Monitoring Systems, J Geophys Res 125:9,doi:10.1029/2020JB020284.

Nakamura, Y., et al. (2022), Structural Anomaly at the Boundary Between Strong and Weak Plate Coupling in the Central-Western Nankai Trough,Geophys Res Lett 49:e2022GL098180. doi:10.1029/2022GL098180.

Qin et al. (2020), High-Density Seismic Refraction Imaging of Plate-Boundary Structures in the Slow Earthquake Gap Zone off Western Kii Penin-sula, Nankai Trough, Geophys Res Lett 48:e2020GL089132. doi:10.1029/2020GL089132

Shiraishi et al. (2020), “Three-dimensional topographic relief of the oceanic crust may control the occurrence of shallow very-low-frequency earth-quakes in the Nankai Trough off Kumano"Earth, Planets and Space, 72:1, doi:10.1186/s40623-020-01204-3.

Tonegawa, T., et al. (2021), Weak faults at megathrust plate boundary respond to tidal stress, Earth Planets Space 73:89. doi:10.1186/s40623-021-01414-3.

Tonegawa, T., et al. (2022b), Fluid Migration Before and During Slow Earthquakes in the Shallow Nankai Subduction Zone, J Geophys .Res127:e2021JB023583. doi:10.1029/2021JB023583

Yamamoto, Y., et al. (2022), Spatio-temporal distribution of shallow very-low-frequency earthquakes between December 2020 and January 2021in Kumano-nada, Nankai subduction zone, detected by a permanent seafloor seismic network, Earth Planets Space 74:14 doi:10.1186/s40623-022-01573-x.

Yokota, Y., et al. (2016). Seafloor geodetic constraints on interplate coupling of the Nankai Trough megathrust zone. Nature 534, 374–377, https://doi.org/10.1038/nature17632Yokota, Y.& Ishikawa, T. (2020). Shallow slow slip events along the Nankai Trough detected by GNSS-A, Sci. Adv. 6, eaay5786, doi: 10.1126/sciadv.aay5786

7 Notice on Using

This cruise report is a preliminary documentation as of the end of cruise.
This report is not necessarily corrected even if there is any inaccurate description (i.e. taxonomic classifications). This report is subject to be revised without notice. Some data on this report may be raw or unprocessed. If you are going to use or refer the data on this report, it is recommended to ask the Chief Scientist for latest status.
Users of information on this report are requested to submit Publication Report to JAMSTEC.

http://www.godac.jamstec.go.jp/darwin/explain/1/e#report
E-mail: submit-rv-cruise@jamstec.go.jp